https://doi.org/10.5194/acp-2022-836
Preprint. Discussion started: 9 January 2023

Atmospheric Chemistry and Physics Discussions

Constraints on simulated past Arctic amplification and lapse-rate feedback from observations

Olivia Linke[1], Johannes Quaas[1], Finja Baumer[1], Sebastian Becker[1], Jan Chylik[2], Sandro Dahlke[3], André Ehrlich[1], Dörthe Handorf[3], Christoph Jacobi[1], Heike Kalesse-Los[1], Luca Lelli[4,9], Sina Mehrdad[1], Roel A.J. Neggers[2], Johannes Riebold[3], Pablo Saavedra Garfias[1], Niklas Schnierstein[2], Matthew D. Shupe[5], Chris Smith[6,7], Gunnar Spreen[4], Baptiste Verneuil[1,8], Kameswara S. Vinjamuri[4], Marco Vountas[4], and Manfred Wendisch[1]

[1]Leipzig Institute for Meteorology, Leipzig University, Leipzig, Germany
[2]Institute of Geophysics and Meteorology, University of Cologne, Cologne, Germany
[3]Alfred Wegener Institute, Helmholtz Centre for Polar and Marine Research, Potsdam, Germany
[4]Institute of Environmental Physics, University of Bremen, Bremen, Germany
[5]Cooperative Institute for Research in Environmental Sciences, University of Colorado Boulder, Boulder, CO, USA
[6]University of Leeds, School of Earth and Environment, Leeds, U.K.
[7]International Institute for Applied Systems Analysis, Laxenburg, Austria
[8]École Polytechnique, Palaiseau, France
[9]Remote Sensing Technology Institute, German Aerospace Centre (DLR), Wessling, Germany

Correspondence: Johannes Quaas (johannes.quaas@uni-leipzig.de)

Abstract. The Arctic has warmed much more than the global mean during past decades. The lapse-rate feedback (LRF) has been identified as large contributor to the Arctic amplification (AA) of climate change. This particular feedback arises from the vertically non-uniform warming of the troposphere, which in the Arctic emerges as strong near-surface, and muted free-tropospheric warming. Stable stratification and meridional energy transport are two characteristic processes that are evoked as causes for this vertical warming structure. Our aim is to constrain these governing processes by making use of detailed observations in combination with the large climate model ensemble of the 6th Coupled Model Intercomparison Project (CMIP6). We build on the result that CMIP6 models show a large scatter in Arctic LRF and AA, which are positively correlated for the historical period 1951–2014. Thereby, we present process-oriented constraints by linking characteristics of the current climate to historical climate simulations. In particular, we compare a large consortium of present-day observations to co-located model data from subsets with weak and strong simulated AA and Arctic LRF in the past. Our results firstly suggest that local Arctic processes mediating the lower thermodynamic structure of the atmosphere are more realistically depicted in climate models with weak Arctic LRF and AA (CMIP6/w) in the past. In particular, CMIP6/w models show stronger inversions at the end of the simulation period (2014) for boreal fall and winter, which is more consistent with the observations. This result is based on radiosonde observations from the year-long MOSAiC expedition in the central Arctic, together with long-term radio soundings at the Utqiaġvik site in Alaska, USA, and dropsonde measurements from aircraft campaigns in the Fram Strait. Secondly, remote influences that can further mediate the warming structure in the free troposphere are more realistically represented by models with strong simulated Arctic LRF and AA (CMIP6/s) in the past. In particular, CMIP6/s models systemically simulate

https://doi.org/10.5194/acp-2022-836
Preprint. Discussion started: 9 January 2023

Atmospheric Chemistry and Physics Discussions

a stronger Arctic energy transport convergence in the present climate for boreal fall and winter, which is more consistent with reanalysis results. Locally, we find links between changes in transport pathways and vertical warming structures that favor a positive LRF in the CMIP6/s simulations. This hints to the mediating influence of advection on the Arctic LRF. We emphasise that one major attempt of this work is to give insights in different perspectives on the Arctic LRF. We present a variety of contributions from a large collaborative research consortium to ultimately find synergy among them in support of advancing our understanding of the Arctic LRF.

1 Introduction

The Arctic region is subject to an amplification of climate change (Serreze and Barry, 2011; Wendisch et al., 2022). Several intertwined processes and feedback mechanisms contribute to the strong Arctic warming. Temperature feedbacks play a crucial role for the Arctic amplification (AA) of global warming (e.g., Pithan and Mauritsen, 2014; Block et al., 2020). We investigate the lapse-rate feedback (LRF) which arises from the vertically non-uniform contribution to the total temperature feedback. This particular feedback contributes at a level that is similar to the surface albedo feedback to AA, but its underlying physical mechanisms are less well understood (Feldl et al., 2020; Lauer et al., 2020; Boeke et al., 2021). Results from the recent multi-climate model ensemble within the 6th Coupled Model Intercomparison Project (CMIP6; Eyring et al., 2016) confirm that the LRF has a unique latitudinal dependence: The multi-model average in Fig. 1a shows a negative LRF in the tropics and large parts of the mid-latitudes, and a positive LRF in the polar regions, primarily die Arctic. Most of the negative feedback contribution comes from the tropical regions, where the warming is amplified in higher altitudes. This enhances the atmospheric long-wave cooling ability towards space.

In the Arctic, the widespread surface-based temperature inversion and limited vertical mixing abilities of the atmosphere cause the major part of the warming to remain in the lower troposphere (Manabe and Wetherald, 1975). This bottom-heavy warming (BHW) is a key feature of the overall positive Arctic LRF (ALRF). Given the muted warming in the free troposphere, the ALRF limits the atmospheric cooling ability in the long-wave radiation spectrum, which ultimately aids the Greenhouse effect. The latitudinal control on the sign of the local feedback makes the LRF an important contribution to AA (Pithan and Mauritsen, 2014; Block et al., 2020).

The ALRF experiences a unique seasonal and spatial variability (e.g., Feldl et al., 2020; Boeke et al., 2021). The major part of the overall positive feedback results from the boreal fall and winter period, where the degree of sea ice retreat has a strong control on the local intensity of the LRF. Local changes in the sea ice concentration are of central importance through changes in the surface turbulent heat fluxes. Primarily the regions with strong sea ice reduction experience an increase in the upward turbulent heating from the ocean, which mediates the local maximum of the winter-time ALRF (Feldl et al., 2020; Linke and Quaas, 2022).

Here, we are interested in the contribution of the LRF to Arctic climate change as observed since 1951. Wendisch et al. (2022) report that in the Arctic (in their study defined as the averaged area north of 60° N), the period of 1991–2021 was warmer by 1.33 K compared to the reference period 1951–1980, which is more than twice the global-mean warming. We make

https://doi.org/10.5194/acp-2022-836
Preprint. Discussion started: 9 January 2023

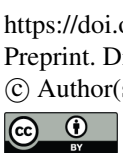

Atmospheric Chemistry and Physics Discussions

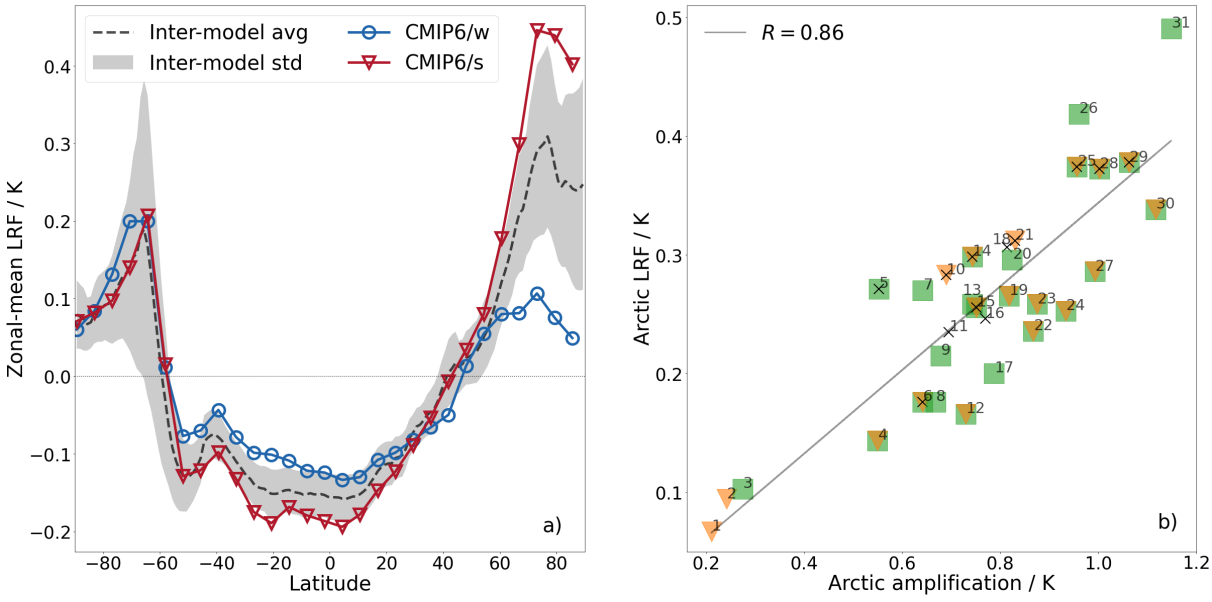

Figure 1. a) Zonal and annual-mean LRF (for the period 1985–2014 with respect to 1951–1980) expressed in surface temperature change units, K. The black dashed line indicates the multi-model average (avg) from all 31 CMIP6 models used in this study. The shaded area gives the inter-model standard deviation (std) around the model mean. The blue lines with circles, and red lines with triangles give the average of the 3 models in our collection with lowest, and highest AA (CMIP6/w, and CMIP6/s), i.e. models 1–3, and 29–31 of Tab. 1, respectively. b) Relationship between ALRF and AA in CMIP6 models. As in a), the model-specific temperature change and feedback is derived for the period 1985–2014 with respect to 1951–1980. Green squares represent models for which monthly, orange triangles for which daily, and black crosses for which 6-hourly output data are available from the CMIP6 archive. For the derivation of model-specific AA and LRF, monthly diagnostics of all models (numbering in panel b corresponds to Tab. 1) have been used.

use of the CMIP6 "historical" simulations with the best estimates of transient climate forcings over the time period of 1850–2014. Here, climate change accounts for the difference between the last 30 years available from the simulations (1985–2014), and an earlier 30 years of the period of interest, 1951–1980. The resulting AA and ALRF are summarised in Fig. 1b, which gives the respective model-specific values as individual scatters. In this study, we define AA as the difference between Arctic (accounting for the area north of 66° N) and global-mean warming.

Given the strong seasonal and spatial variability of the ALRF, it is useful to distinguish different seasons as well as different surface-types for a detailed analysis. For the former point, our results are present for different times of the year, depending on the observational constraints. We distinguish boreal spring, summer, fall, and extended winter as April-May-June (AMJ), July-August-September (JAS), October-November (ON), and December-January-February-March (DJFM), respectively. Even though all seasons are considered, we mostly focus on the winter season, where the ALRF is stronger. For the latter point of the surface-control on the ALRF, it is most relevant whether the atmospheric column is over sea ice or open ocean. Since we focus

https://doi.org/10.5194/acp-2022-836
Preprint. Discussion started: 9 January 2023

Atmospheric Chemistry and Physics Discussions
Open Access
EGU

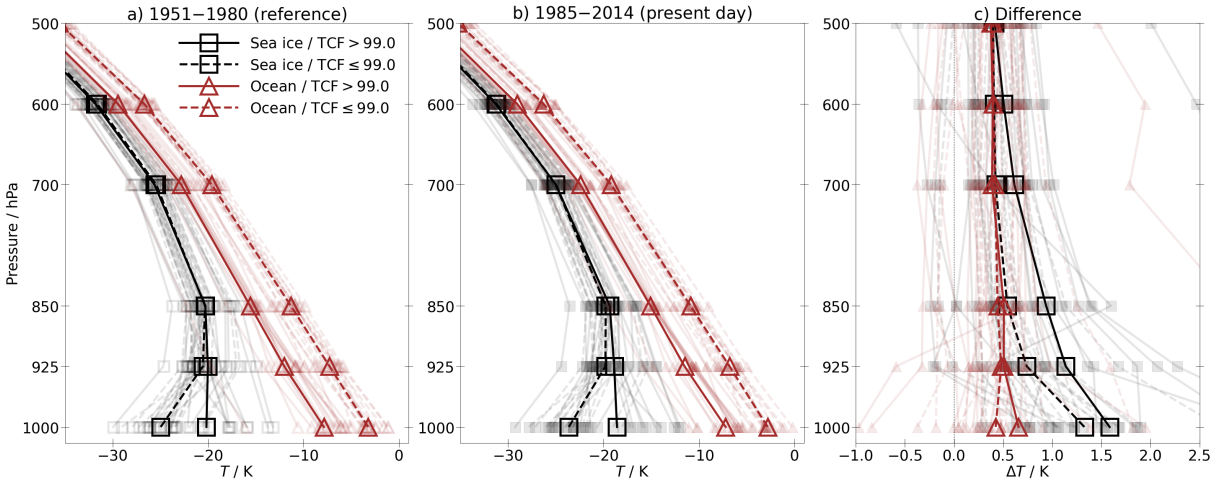

Figure 2. Temperature profiles derived from monthly-mean CMIP6 data a) during the reference period 1951–1980, and b) present-day period 1985–2014, as well as c) the difference between the later and earlier period. The season is DJFM. Temperature profiles are derived over sea ice and ocean surfaces for highly cloudy (overcast) conditions with total cloud fractions (TCFs) of TCF $> 99\,\%$, and non-overcast conditions, TCF $\leq 99\,\%$, in the columnar monthly-mean files, respectively. The sea-ice concentration threshold is $15\,\%$, above which we define the ocean surface as sea-ice covered. Model grid points are selected as either sea ice or open ocean where these conditions are fulfilled throughout the period 1951–2014, i.e., we do not account for areas that transition from sea ice to open ocean. The curves show the multi-model average (thicker curves), and individual models (thin, shaded curves). Note that not all 31 models are included here, as not every model gave an output profile for each of the four classifications by surface-type and cloudiness.

mainly on a model-to-observation comparison over the Arctic ocean, we exclude the influence of snow-covered vs. snow-free land here.

We firstly motivate the influence of the surface type, and additionally cloudiness on the ALRF during extended winter, purely in CMIP6 data: Figure 2 shows temperature profiles in the lower and middle troposphere, filtered for different conditions. Profiles are categorised into two surface types (sea ice, ocean) and two cloud conditions, based upon a threshold in the total cloud fraction (TCF) within the model grid-cell (TCF $> 99\,\%$, or TCF $\leq 99\,\%$). Therefore, we distinguish four different cases: sea ice / TCF $> 99\,\%$, sea ice / TCF $\leq 99\,\%$, ocean / TCF $> 99\,\%$, and ocean / TCF $\leq 99\,\%$. The sea ice concentration threshold of $15\,\%$ is used to distinguish the sea ice from the open ocean states. The categorisation by cloudiness has the aim to separate the particularly cloudy (overcast) conditions from the rest. We discuss the choice of the TCF threshold later on in the text. From distinguishing by surface-type and cloudiness, we motivate observational constraints with the following conclusions from purely model-based outputs:

- Reference and present-day periods: For non-overcast cases (TCF $\leq 99\,\%$), the contrast in surface temperature over sea ice and open ocean dominates the temperature profiles. Over sea ice, strong surface inversions exist while over the relatively warm ocean, the atmospheric boundary layer is well mixed. For overcast cases (TCF $> 99\,\%$), the strong cloud

https://doi.org/10.5194/acp-2022-836
Preprint. Discussion started: 9 January 2023


Atmospheric Chemistry and Physics Discussions

cover reduces the surface temperature contrast between sea ice and open ocean. Over sea ice, cloud top cooling leads to a top-down mixing of the atmospheric boundary layer, which weakens the surface inversion. Some models show a lifted inversion (e.g., CESM2; not shown). Over open ocean, both cloud conditions show a similar stability, but the highly-clouded profile is colder throughout the lower troposphere. This is due to the fact that these cases have their peak in relative occurrence more concentrated towards the sea ice edge (not shown here) compared to the less clouded profiles over ocean.

– Present-day minus reference period: The open-ocean areas show no substantial change in lapse-rate, i.e. no strong LRF results from both cloud conditions over open ocean. However, there is a strong warming near the surface over sea ice for both highly- and less-clouded conditions as compared to over open ocean. The overall warming in the overcast cases is more pronounced than for other conditions, likely due to the fact that these cases appear mostly over the strong-ice melt areas of the Barents-Kara sea (not shown here), which have a notoriously strong warming. However, it is only under overcast conditions that this enhanced warming signal extends up into the mid-troposphere. The gradient of the temperature change from the surface to 850 hPa over sea ice is larger under less-clouded conditions relative to overcast conditions. Thereby, more clouds reduce bottom-heavy warming with respect to the lower troposphere up to 850 hPa. However, considering the entire troposphere (extending from the surface to 300 hPa in our approach), the overall columnar LRF accounting for the lapse-rate change in each layer, is stronger for overcast profiles.

Summarising this introduction to the state of the art, climate models imply a large role of inversion, surface type and clouds for the evolution of the Arctic temperature profile with warming. In addition to that, the thermal structure of the atmosphere can be impacted by remote processes like poleward energy transport. Those controls motivate to investigate if detailed observations (or reanalyses) can be used as constraints, based upon the CMIP6 inter-model spread in AA and ALRF (Fig. 1b).

The key ideas are:

1. The Arctic LRF is largely controlled by local influences on the surface-near thermodynamic structure: The lack of vertical mixing in the Arctic boundary layer is a key to understand and adequately model the ALRF. As a result, one focus will be on the evaluation of simulated inversion strengths by various means. Additionally, the ALRF is largely depending on the underlying surface type. Most importantly, the strong contrast in LRF over sea-ice and open-ocean surfaces motivates an evaluation of the simulated warming that is expected through sea ice retreat.

2. The meridional transport of energy in the Arctic free troposphere undergoes a change due to Arctic warming and may amplify or dampen the ALRF by energy advection at different altitudes.

3. The lapse-rate change is linked to cloudiness and vertical mixing strength in the atmospheric column. A further aim is to motivate an assessment of how clouds and boundary-layer dynamics shape changes in the lapse rate by a vertical re-distribution of the warming.

We address point 1 and 2 by comparing present-day (or historical changes in) observations or reanalyses with co-located model data. The constraint is based on the separation of the co-located model data into a subset of models with either weak or strong

https://doi.org/10.5194/acp-2022-836
Preprint. Discussion started: 9 January 2023


Atmospheric Chemistry and Physics Discussions

simulated past AA (and ALRF given their high inter-model correlation; Fig. 1b). By identifying differences between both model subsets, and falsifying one or the other based upon observations, we link characteristics of the current climate to long-term historical climate simulation. This allows us to evaluate the performance of CMIP6 models, and to constrain both local and remote processes mediating the ARLF. Point 3 on the role of clouds and boundary-layer dynamics is treated separately from this process-oriented constraint. Our model-based results in Fig. 2 are thereby linked to a deeper study of these perspectives in large-eddy simulations.

We note that this work aims to provide insights in different perspectives on the Arctic lapse rate and the LRF. We bring together a variety of contributions from a large research consortium, and ultimately seek to find synergy among them in support of advancing our understanding of the LRF in the Arctic.

In Section 2 we firstly elaborate on how the Arctic LRF is calculated from climate model diagnostics and radiative kernels, and how to facilitate a constraint based upon this. Secondly, the different observational data sets and individual methods are described. Section 3 evaluates the performance of the two CMIP6 model subsets to simulate processes governing the Arctic LRF, based on the observations introduced in Section 2. In the discussion, we further explain the differences between both model subsets and link our results to the historical climate simulations, which is equivalent to our constraint. Our final conclusions revisit the key hypotheses 1–3.

2 Methods

To address the objectives of this study, we evaluate the performance of a subset of CMIP6 models with a wide range of observables in different parts of the Arctic. From CMIP6, we use historical simulations with the best estimates of the transient climate forcings during 1850–2014 (Eyring et al., 2016). In this study, we focus on the period 1951–2014. While monthly-mean data is available for most CMIP6 models, only a few models provide all diagnostics necessary for comparing data at higher time resolutions. Therefore, we define three different model data sets at different time resolutions: monthly, daily, and 6-hourly. We specify the models that provide all necessary diagnostics per time-resolution group in Table 1. The model data for each of these time-resolution groups are further broken down into a respective subset that simulates an either weak, or strong historical AA and ALRF (CMIP6/w, or CMIP6/s, respectively). For CMIP6/w, and CMIP6/s subsets we group together the three models with lowest, and highest simulated AA, respectively (see Table 1 for details). Note that not all models in Table 1 are used for the comparison with monthly-mean data sets. However, for all 31 models, the model-specific ALRF and AA were calculated based on monthly temperature diagnostics. This is due to the fact that temperature data are more commonly provided among the models than other diagnostics (e.g., sea ice concentration).

In each comparison step, we use a specific observational data set to evaluate the performance of the respective CMIP6/w and CMIP6/s subset, and to constrain one key process mediating the ALRF. The location of the observational sites are summarised in Fig. 3. The model-to-observation (or model-to-reanalysis) comparisons include the following:

- We compare temperature inversion strengths measured during the Multidisciplinary drifting Observatory for the Study of Arctic Climate (MOSAiC; Shupe et al., 2022) to corresponding CMIP6 data. The color coding in Fig. 3 shows the

https://doi.org/10.5194/acp-2022-836
Preprint. Discussion started: 9 January 2023

Atmospheric Chemistry and Physics Discussions

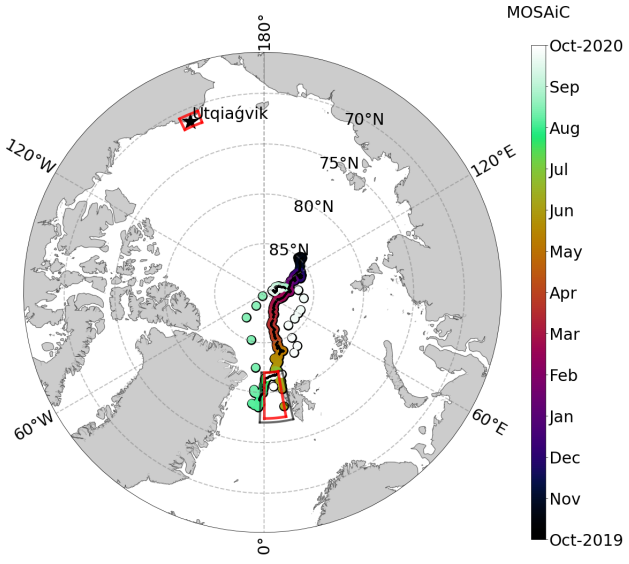

Figure 3. The Arctic region north of 66° N summarising all domains considered for comparing observations and reanalyses to CMIP6. Color coding represents the location of the *RV Polarstern* drift as a function of time from October 2019 to October 2020 during the MOSAiC expedition. Black dots in the track represent location and time of the observational data set used in this study (Sec. 2.2). The ARM site at Utqiaġvik, NSA is marked by a star (Sec. 2.3). The dropsonde domain is the enclosed area in the Fram Strait marked by the grey trapeze (Sec. 2.4). The regions around Utqiaġvik and the Fram Strait discussed in Sec. 2.5 are marked by red trapezes. The entire area north of 66° N is used for deriving Pan-Arctic averages of Arctic LRF and AA (Sec. 2.1). Additionally, we consider the net energy transport across the Arctic boundary, and the long-wave radiation budget at TOA within this area (Section 2.6 and 2.7, respectively).

drift of the research vessel *RV Polarstern* during MOSAiC from October 2019 to October 2020. More information is given in Section 2.2.

- Complimentary to MOSAiC, we further use inversion data from long-term radiosonde observations at the Atmospheric Radiation Measurement (ARM) site at Utqiaġvik, Alaska, USA (see Section 2.3 for details).

- We further analyse measurements of temperature profiles by dropsondes released from research aircraft during measurement campaigns in the Fram Strait (gray box in Fig. 3). More information about the campaign data is provided in Section 2.4.

- In the context of remote controls on the ALRF, we relate the depth of the Arctic warming at the observational sites at Utqiaġvik and the Fram Strait (enclosed by red sectors in Fig. 3) with preferred large-scale atmospheric circulation regimes over these regions. Further information is given in Section 2.5.

https://doi.org/10.5194/acp-2022-836
Preprint. Discussion started: 9 January 2023

Atmospheric Chemistry and Physics Discussions

– To broaden the perspective of advective controls, we derive the Pan-Arctic poleward energy transport across the Arctic boundary at 66° N latitude, which encloses the entire area illustrated in Fig. 3. The methodology is further specified in Section 2.6.

– Finally, the LRF as a positive radiative feedback in the Arctic locally enhances the Greenhouse effect. Therefore, we relate its strength to changes in the long-wave radiation budget at the top of the atmosphere (TOA). Again, we consider the area north of 66° N to derive Pan-Arctic averages. Details are described in Section 2.7.

– In an outlook perspective, to augment the observational data sets derived during MOSAiC, we further conducted daily Large-Eddy Simulations (LES) for the whole MOSAiC drift (Section 2.8). These simulations aim to discuss processes at turbulence- and cloud-resolving scale, as they are largely underrepresented in the literature covering the Arctic LRF.

2.1 The Arctic LRF and Arctic amplification in CMIP6

To facilitate constraints on the past AA and ALRF, we first calculate a model-specific AA and ALRF value from monthly-mean temperature fields for all 31 climate models considered in this study. We define the degree of AA by subtracting the global-mean temperature change of the near-surface atmosphere, ΔT_s, from the respective Arctic-mean warming. Arctic mean values account for the averaged area north of 66° N.

The LRF arises from tropospheric warming that is vertically non-uniform. The change in temperature profiles is calculated for the averaged period of the last 30 years of the historical simulations (1985–2014) compared to 1951–1980. The feedback is derived from pre-computed radiative kernels which give the change in TOA radiation balance due to a perturbation of the temperature by 1 K. We considered radiative kernels from the CAM5 (Pendergrass, 2017), GFDL AM2 (Feldl et al., 2017), ERA-Interim (Huang et al., 2017), and HadGEM3-GA7 (Smith et al., 2020) climate models. However, due to the large consistency amongst the kernel-specific results, we stick to the HadGEM3-GA7 radiative kernel for simplicity. The feedback parameter λ is defined as

$$\lambda = \frac{\partial R}{\partial X}\frac{\Delta X}{\Delta T_\mathrm{s}}, \tag{1}$$

with $\frac{\partial R}{\partial X}$ representing the kernel. ΔX gives the change in temperature profile that deviates from ΔT_s. The LRF is calculated by applying Eq. (1) and integrating over the troposphere. We derive the tropopause following Soden and Held (2006), by defining the 100 hPa pressure level as tropopause at the equator, and using a linear slope (according to geographical latitude) down to 300 hPa at the poles.

The feedback parameter λ has units of $\mathrm{Wm^{-2}K^{-1}}$. We redefine the feedback parameter as a warming contribution to ΔT_s, by using the local energy budget following several prior studies (Lu and Cai, 2009; Crook et al., 2011; Feldl and Roe, 2013; Taylor et al., 2013; Pithan and Mauritsen, 2014; Goosse et al., 2018; Hahn et al., 2021):

$$0 = F + \left(\sum_i \lambda_i + \lambda_\mathrm{P}\right)\Delta T_\mathrm{s} + \Delta\mathrm{OHU} + \Delta\mathrm{AHT} = F + \left(\sum_i \lambda_i + \overline{\lambda_\mathrm{P}} + \lambda'_\mathrm{P}\right)\Delta T_\mathrm{s} + \Delta\mathrm{OHU} + \Delta\mathrm{AHT}. \tag{2}$$

https://doi.org/10.5194/acp-2022-836
Preprint. Discussion started: 9 January 2023

Atmospheric Chemistry and Physics Discussions

The local energy budget in Eq. (2) describes the energetic contributions of the radiative forcing F, the feedbacks ($\lambda_i \Delta T_\mathrm{s}$) and the Planck response ($\lambda_\mathrm{P} \Delta T_\mathrm{s}$), as well as the ocean heat uptake (ΔOHU), and the anomalous atmospheric heat transport convergence (ΔAHT). The second step splits the Planck feedback in its global-mean value, $\overline{\lambda_\mathrm{P}}$, and the spatially resolved deviation from it, $\lambda'_\mathrm{P} = \lambda_\mathrm{P} - \overline{\lambda_\mathrm{P}}$. Therefore, we can derive the warming contributions to ΔT_s of forcings and feedbacks by dividing each term in Eq. (2) by the global-mean Planck feedback ($\overline{\lambda_\mathrm{P}}$):

$$\Delta T_\mathrm{s} = -\frac{\left(F + \Delta\mathrm{OHU} + \Delta\mathrm{AHT}\right)}{\overline{\lambda_\mathrm{P}}} - \frac{\left(\lambda'_\mathrm{P} + \sum_i \lambda_i\right) \Delta T_\mathrm{s}}{\overline{\lambda_\mathrm{P}}}. \tag{3}$$

In that form, each of the individual contributions on the right-hand side add up to the full change in T_s. In our study however, we only consider the contribution of the LRF. This approach offers the advantage of emphasising the physical connection between local radiative fluxes and the local temperature change by climate feedbacks (Feldl and Roe, 2013).

2.2 Temperature inversions from radio soundings during MOSAiC

During the MOSAiC expedition between October 2019 and October 2020, the *RV Polarstern* drifted within the central Arctic sea ice. During the expedition, among others, vast atmospheric measurements were carried out (Shupe et al., 2022). In this study, we analyse thermodynamic profiles from Vaisala RS41-SGP radiosondes that were launched at least four times per day (Maturilli et al., 2021). In order to estimate inversion strengths from the soundings, we additionally employ concurrent 2-m temperature (T2m) measurements from the nearby MOSAiC ice camp (Cox et al., 2021), since the soundings were launched from the ship's helicopter deck approximately 10-m above the ice, thereby missing the lowermost meters of the atmospheric column. In addition, using the T2m tower data reduces the impact of the ship on the near-surface temperature. We derive the inversion strength as the difference between the temperature-profile maximum (Tmax; between the surface and 250 hPa) and T2m.

The temporal resolution for the inversion data follows the frequency of radiosonde launches during the MOSAiC expedition (approximately every 6 hours). For the model-to-observation comparison, we consider 6-hourly temperature diagnostics for the period 2010–2014 that were co-located to MOSAiC in space and time. Since the climate models are free-running coupled models, it is not essential to use the exact years of 2019 / 2020 (assuming that 2010–2014 and 2019–2020 are roughly the same climate). Instead, the correct time (i.e., time of day and season), and spatial location are co-located. The model output data is chosen corresponding to which time step and grid-box midpoint is closest to each individual MOSAiC radiosonde launch time. Essentially, the model data "follow" the MOSAiC track in space and time of the year. We equally derive the temperature inversion in the model data as the difference between Tmax and T2m.

Note that there are no inversion data available at MOSAiC between 9 May 2020 to 10 June 2020, and 29 July 2020 to 25 August 2020 when the ship was in transit through the sea ice. Figure 3 shows the entire drift of *RV Polarstern* with time attribution according to the radiosonde launches as color coding. The black dots following the drift depict the locations where observational data was available for our study (limited by the availability of T2m tower data).

https://doi.org/10.5194/acp-2022-836
Preprint. Discussion started: 9 January 2023


Atmospheric Chemistry and Physics Discussions

2.3 Temperature inversions from radio soundings at Utqiaġvik (NSA)

The ARM program organised by the U.S. Department Of Energy (DOE) provides a long-term record of atmospheric observations from permanent and mobile measurement sites around the world (Mather and Voyles, 2013). One ARM site that is particularly relevant for Arctic studies is the North Slope of Alaska (NSA) in Utqiaġvik, Alaska, USA. With a geographical location of 71.23° N and 156.61° W, the NSA site is one of the most important sources for long-term western Arctic atmospheric observations, which makes it ideal for climate studies.

For this study we use atmospheric temperature profiles from radiosonde launches performed at the NSA site. The so-called interpolated sounding (INTERPSONDE) Value Added Product is obtained after linearly interpolating the atmospheric state variables from consecutive soundings into a fixed 2-D time-height grid. The grid's temporal resolution is 1 min. The vertical resolutions varies with the altitude, ranging from 20 m in the lowest 3.5 km, to 50 m between 3.5–5 km, to 100 m between 5–7 km, and to 200 m between 7–20 km altitude, respectively. It is important to mention that the input for the INTERPSONDE-product comprises only data from quality controlled soundings and precipitable water vapour estimated from microwave radiometer measurements, and it does not incorporate ancillary observations from surface or tower meteorological observations. The INTERPSONDE-product's fixed 2-D grid facilitates the comparison with weather and climate models. Radiosonde data for the NSA site are available since April 2002, with a varying 2 to 4 launches per day (Jensen et al., 1998). The overlapping time period available for analysis constrains the data set to the range of April 2003 to December 2014.

Once CMIP6 model output and NSA radiosonde data are processed to be comparable, we estimate the inversion strength as in the MOSAiC comparison, as the difference between Tmax and T2m, and at 6-hourly time resolution. We only take into account inversion strengths larger than 0.5 K to dismiss cases that resemble adiabatic lapse-rates.

2.4 Temperature profiles from dropsondes in the Fram Strait

The relationship between the ALRF and the strength of sea ice retreat motivates the assessment of temperature profiles above both sea-ice and open-ocean surfaces, as well as their differences. For this purpose, measurements of dropsondes released from research aircrafts in the Fram Strait are analysed. The dropsondes deliver atmopsheric profiles for altitudes below the launch location. The limited flight altitude of the employed research aircrafts constrains the maximum altitude of the resulting temperature profiles to about 3 km. The measurements presented here were performed during March to ensure similar thermodynamic conditions compared to the extended winter season, DJFM. In total, 52 dropsondes are analysed, which were launched mainly in an area between 77–82° N and 2° W–13° E (see Fig. 3) during the following three campaigns: eight sondes during the Radiation and Eddy Flux Experiment (REFLEX, performed in March 1993; Lüpkes and Schlünzen, 1996), 22 sondes during the Spring Time Atmospheric Boundary Layer Experiment (STABLE, performed in March 2013; Lüpkes et al., 2021), and 22 sondes during the Airborne measurements of radiative and turbulent FLUXes of energy and momentum in the Arctic boundary layer campaign (AFLUX, performed in March/April 2019; Becker et al., 2020).

For surface type classification, the sea ice concentration at the dropsonde launch location was obtained from satellite observations (Kern et al. (2020) for REFLEX, and Melsheimer and Spreen (2019) for STABLE and AFLUX). If the sea ice

https://doi.org/10.5194/acp-2022-836
Preprint. Discussion started: 9 January 2023


Atmospheric Chemistry and Physics Discussions

concentration was below 15 %, a profile is considered to represent conditions over open ocean, while a sea ice concentration above 85 % corresponds to sea-ice covered ocean. Thereby, we exclude data from 6 dropsondes that were launched over the marginal sea ice zone (15–85 %) in this analysis, which is designed to obtain a clear signal for the difference between sea ice and open ocean.

As for MOSAiC and NSA, the model-to-observation comparison applies data with 6-hourly time resolution for 2010–2014 in the model output. Similar to the observations, the temperature profiles from the models were grouped into open ocean and sea ice conditions based on the model sea ice concentration at the respective grid cell. The location of the sea ice edge varies significantly among the models. To reduce the impact of the different distances to the sea ice edge on the thermodynamic profile, grid points with a distance of more than 250 km to the 50 % isoline of sea ice concentration are excluded from the analysis.

2.5 The role of advective heating

Not only can atmospheric stability and sea-ice loss mediate the thermodynamic structure of the atmosphere, but also remote influences. Here, we link the vertical structure of Arctic warming to large-scale atmospheric circulation regimes over the regions of the Fram Strait and Utqiaġvik (marked in Fig. 3).

We identify atmospheric circulation regimes in reanalysis data by applying a k-means clustering algorithm to daily mean sea-level pressure (SLP) fields over the North-Atlantic-Eurasian region (30–90° N, 90° W–90° E) and over the North-Pacific region (30–90° N, 90° E–90° W) for the extended winter season (DJFM). For the reanalysis data, the 5th generation reanalysis of the European Centre for Medium-Range Weather Forecasts is employed (ERA5; Hersbach et al., 2020). We follow the approach described in Crasemann et al. (2017) and determine the circulation regimes in a reduced state space spanned by the five leading empirical orthogonal functions (EOFs; Dawson and Palmer, 2015). The coordinates in this state space are provided by the corresponding unnormalized Principal Component (PC) time series. For the subsequent clustering, the number of clusters k has been set to $k = 5$ following Crasemann et al. (2017).

For the analysis of the CMIP6 data we apply a projection approach described in Fabiano et al. (2021) where the state space spanned by the ERA5-EOFs serves as the reference state space for the CMIP6 simulations. The coordinates for each simulation are provided by projecting the SLP anomaly data onto the reference state space, obtaining five Pseudo-PCs, for each model simulation. Based on these Pseudo PCs, each day of the respective model simulation is assigned to the closest centroid of the five ERA5 reference clusters. The advantage of this approach is the consistent definition of the atmospheric circulation regimes.

In order to relate the occurrence probability of each circulation regime i (P_i, $\mathrm{i} = 1, ..., 5$) to the vertical structure of the warming at the observational sites, we applied a Multi-Nomial Logistic Regression (MNLR) approach. This approach was used by e.g. Detring et al. (2021) to study recent trends in blocking probabilities, but it is also suitable for the multi-class problem of describing P_i in dependence of some covariates. The basic idea of MLNR is to describe the log-odds (defined as the logarithm of the chance of observing a distinct regime with respect to a predefined base-line regime) as a linear combination of the covariates. For our analysis, the covariates comprise the 2-m temperature (T2m), the mid-tropospheric temperature at

https://doi.org/10.5194/acp-2022-836
Preprint. Discussion started: 9 January 2023


Atmospheric Chemistry and Physics Discussions

500 hPa (T500), and time. T2m and T500 are averaged values over the region around the respective measurement site. Finally, the relationship between the occurrence probability of each circulation regime and the warming structure is expressed as a 2-dimensional PDF dependent on T2m and T500 changes.

We henceforward refer to an increase in T2m, and T500 with time as bottom-heavy warming, and top-heavy warming, respectively. We constrain the remote influence of advective heating on the ALRF by a model-to-reanalysis comparison, using ERA5 and CMIP6 models with daily output data as specified in Table 1.

2.6 Pan-Arctic meridional energy transport convergence

Changes in poleward energy transport and its spatial pattern can affect the LRF in the Arctic by modifying the atmospheric downwelling radiative flux (Hegyi and Deng, 2017; Hegyi and Taylor, 2018). Here, we use the meridional gradient of the TOA net radiative flux (solar+terrestrial) as a proxy to determine poleward energy transport convergence in CMIP6 and ERA5. Only CMIP6 models with daily diagnostics of the TOA net radiative flux were included in this part of the analysis.

The meridional gradients of the daily fields were calculated at the Arctic boundary (66° N) during the last 15 years of CMIP6 simulations (2000–2014). We use the derived longitudinal profiles of the meridional TOA net radiative flux gradient at 66° N to estimate energy transport across 66° N at given longitude. In our analysis, a positive meridional gradient of the TOA net radiative flux accounts for poleward energy transport. The net poleward energy transport convergence in the polar cap is derived by zonally averaging over the Arctic boundary. For our constraint, we compare the transport convergence at present-climate state in a model-to-reanalysis comparison. Due to the larger amount of model data available in the subset with daily resolution (Table 1), we further calculate inter-model correlation coefficients for the entire collection of models.

In a final step, we determine the Wasserstein distance (WSD; a measure to quantify the similarities between two functions; Rüschendorf, 1985) between the models and ERA5 longitudinal transport profiles to depict how well individual CMIP6 models reproduce ERA5 data. Thereby, we also consider the inter-model correlation coefficients between AA / ALRF and the WSD (between the CMIP6 and ERA5 transport patterns).

For determining statistical significance in our analysis, a bootstrap method based on 10000 samples was used. Correlation coefficients with the two-tailed p-value less than 0.05 were considered statistically significant.

2.7 Pan-Arctic outgoing long-wave radiation at the TOA

As an attempt to constrain the past ALRF and AA incorporating all mediating processes introduced so far, we assess changes in the outgoing long-wave radiation (OLR) at TOA. Therefore, we use a satellite-based record of all-sky broadband radiation fluxes (Stengel et al., 2020). These are derived from the Advanced Very High Resolution Radiometer (AVHRR) afternoon orbit (PM) sensors aboard the Polar Operational Environmental Satellite (POES) missions. Details on the derivation of the broadband spectral fluxes can be found in (Henderson et al., 2013).

The difference in the long-wave radiation budget at the TOA is calculated between the averaged period 2000–2014 and 1982–1996. Thereby, we do not cover the entire period of historical CMIP6 simulations ongoing from 1951 to address the change (like in Section 2.5), but instead use the overlap period between the beginning of the satellite record (1982) and the end

https://doi.org/10.5194/acp-2022-836
Preprint. Discussion started: 9 January 2023


Atmospheric Chemistry and Physics Discussions

of the historical CMIP6 simulations (2014). For our model-to-observation comparison, we derive linear trends from changes in the OLR flux at the TOA for both data sets.

2.8 The role of advection, clouds and entrainment in large-eddy simulations (LES)

While the MOSAiC observational data sets (partly addressed in Section 2.2) are unprecedented in their coverage of the low level thermal structure in the central Arctic, various aspects that play a key role in the ALRF were not continuously sampled. These include processes such as turbulent entrainment driven by cloud top cooling across shallow liquid layers. To augment the observational data set, we conduct daily LES for the whole MOSAiC drift, at turbulence- and cloud-resolving scales. The four-dimensional output of these simulations is used as a virtual laboratory to address how small-scale boundary layer processes affect the thermal structure of the lower atmosphere within a heat budget framework. Covering the full MOSAiC drift with such simulations is a significant computational effort and goes far beyond the more common application of LES for short, single case studies. The added value of this effort is that it allows for bridging the gap between small-scale, fast-acting atmospheric boundary-layer processes and long-term means at climate time-scales (Neggers et al., 2012).

The daily LES experiments for MOSAiC were conducted with the DALES code (Heus et al., 2010). The simulated domain is Eulerian, situated around the location of the *RV Polarstern*. The domain size is $0.8 \times 0.8 \times 12\,\mathrm{km}^3$, discretised at a grid-size of $8 \times 8 \times 288$. The horizontal grid-spacing is $100 \times 100\,\mathrm{m}^2$, while for the vertical dimension a telescopic grid is used featuring a vertical resolution of $10\,\mathrm{m}$ across the lowest $2\,\mathrm{km}$. A previous LES study using such micro-grid LES experiments (Neggers et al., 2019) showed that at this resolution and domain size, the turbulent entrainment flux is sufficiently resolved. We thus achieve an optimal balance between computational efficiency and spatial resolution to serve our research goals. Subgrid transport is represented using a turbulent kinetic energy (TKE) scheme, while cloud microphysics are represented using the bulk double moment mixed-phase scheme as described by Seifert and Beheng (2006), applied to five hydrometeor species. While the Cloud Condensation Nuclei (CCN) concentration is prognostic, affected by processes such as advection, diffusion and microphysics, the concentration of Ice Nucleating Particles (INP) is constant. The radiation is interactive with the model state, as are the surface turbulent fluxes.

The experiments are initialized with the 11 UTC radiosonde profile, interpolated onto the LES grid. Observed CCN (Koontz and Uin, 2016) and INP (Creamean, 2019) concentrations at the surface are used to initialize the associated profiles. The lower boundary condition consists of a prescribed observed skin temperature of sea ice (Reynolds and Riihimaki, 2019) and open water, combined through the observed sea ice fraction. The impact of processes larger than the domain size is represented through prescribed forcings for momentum, temperature and water vapour, derived from ERA5 following the method described by Van Laar et al. (2019) and Neggers et al. (2019). Profiles for horizontal advection tendencies are prescribed, and applied homogeneously in the grid. Vertical advection relies on a prescribed profile of large scale vertical motion, acting on the model state. Composite forcing is applied, meaning that it is time-constant and consists of profiles time averaged over the first 11 hours of each day at the *RV Polarstern* location. As a result, the simulation can equilibrate after spin up. Nudging is applied above the thermal inversion that marks boundary layer top, with nudging linearly increasing in intensity across a $1\,\mathrm{km}$ deep

https://doi.org/10.5194/acp-2022-836
Preprint. Discussion started: 9 January 2023


Atmospheric Chemistry and Physics Discussions

transition layer towards full nudging above, at a relaxation timescale of 1800 s. Below the inversion, no nudging is applied, leaving the turbulence and clouds free to evolve.

3 Results

In the following, we revisit all aspects of the present climate system introduced in Section 2 in the scope of a model-to-observation (or reanalysis) comparison. We first present the basis on which our constraints are built in Section 3.1: The large spread among CMIP6 models in simulating the magnitude of ALRF and AA. Following that, we compare each individual observational/reanalysis data set to co-located weak and strong-AA model output data, and falsify either one or the other. We consider first the local, surface-near Arctic processes in Section 3.2 to 3.4 by comparing temperature data from radio soundings and dropsondes to the co-located model data. We then transition from local to remote processes, that can further affect the higher troposphere, in Section 3.5 and 3.6. Section 3.7 serves as a summarising result of the individual aspects, by considering changes in the long-wave radiation budget at the TOA. Section 3.8 gives an outlook on the role of clouds and boundary layer dynamics.

3.1 Relation between LRF and AA in CMIP6 models

Firstly, the scatter plot in Fig. 1b shows the spread in AA among climate models, which linearly relates to their spread in ALRF (linear correlation coefficient $R = 0.86$). Thereby, models with a higher magnitude of AA have a stronger positive ALRF. Secondly, Fig. 1a shows a clear distinction of the CMIP6/w and CMIP6/s model subsets from the multi-model mean, and the results from these models naturally fall outside the ensemble standard deviation. In addition, the stronger contribution to AA from the CMIP6/s collection comes from the combination of both a more negative radiative feedback in the tropics, and a more positive Arctic LRF. This, however, does not necessarily relate to the intermodel spread in global warming: The linear correlation coefficient between global warming and ALRF/AA is 0.45/0.51, respectively.

All models used in this study are specified in Table 1, including the model-specific AA and ALRF, corresponding to Fig. 1b. Again, we use different models for representing CMIP6/w and CMIP6/s model subsets, depending on the time resolution. The model usage is specified in Table 1 by a superscript in the model acronym. Note that individual time-resolution groups always apply the same models. For instance, Section 2.2–2.4 compare model and observational data at 6-hourly resolution. Thereby, the CMIP6/w subset includes data from the SAM0-UNICON, MPI-ESM-1-2-HAM and AWI-ESM-1-1-LR, and CMIP6/s from CNRM-ESM2-1, CNRM-CM6-1-HR and IPSL-CM6A-LR model, respectively.

3.2 Temperature inversions from radio soundings during MOSAiC

In a first step, we evaluate the ability of CMIP6 models to simulate the omnipresent surface-based temperature inversion in the Arctic. Figure 4 shows the comparison between inversion measurements during the MOSAiC expedition, and co-located simulated inversion data for the CMIP6/w and CMIP6/s subsets, respectively.

https://doi.org/10.5194/acp-2022-836
Preprint. Discussion started: 9 January 2023

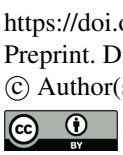

Atmospheric Chemistry and Physics Discussions

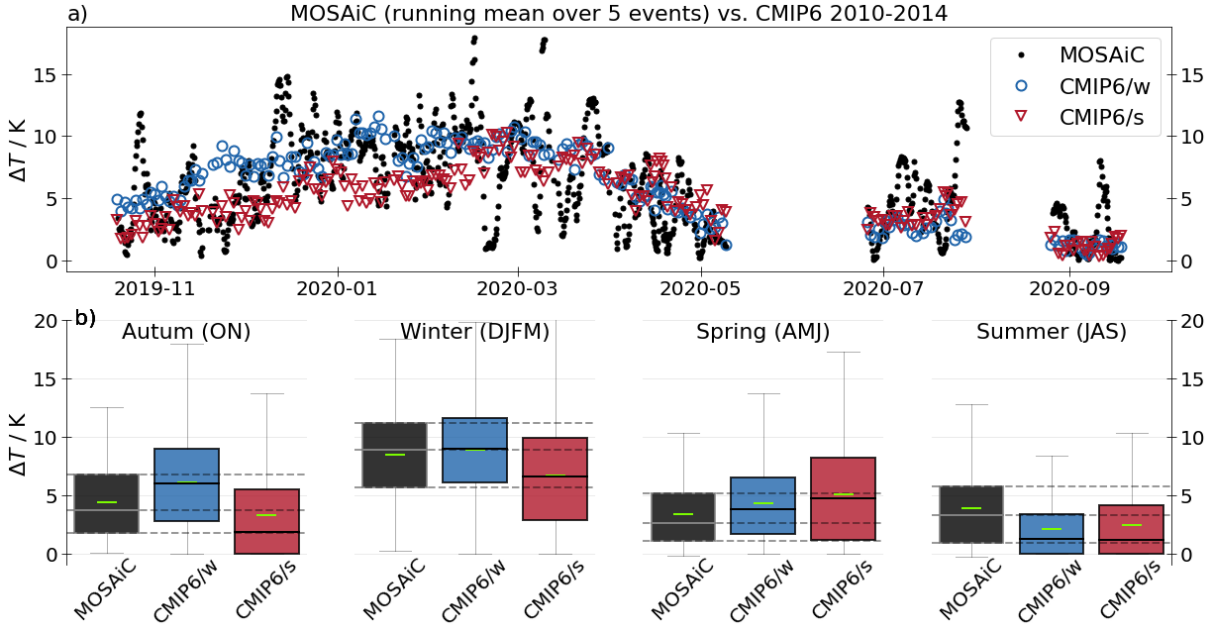

Figure 4. a) Inversion strengths ΔT obtained from radio soundings during the MOSAiC expedition, and for the model subsets CMIP6/w and CMIP6/s, respectively. The time series of radio soundings during MOSAiC is given as rolling average over 10 launches. b) Seasonal inversion strengths ΔT as box plots, corresponding to panel a. Boxes show the 25 to 75-percentile of the data, whiskers the 5 to 95-percentiles, grey horizontal lines in the boxes the median values, and green horizontal lines the mean values. MOSAiC data was collected during Oct 2019 to Oct 2020, and is compared to co-located 6-hourly model data in the period of 2010–2014. Details on the data processing are given in Section 2.2.

The time series in Fig. 4a depicts, on average, a stronger inversion for the CMIP6/w subset during boreal fall (ON) and extended winter (DJFM). In turn, during spring (AMJ), the CMIP6/s subset shows slightly stronger inversions, on average. For summer (JAS), both model groups have similar inversion strengths. The differences between both model subsets are only significant during ON and DJFM.

We propose the following to explain the relation between present-day inversion and historical LRF in the Arctic: The stronger inversion in CMIP6/w in the present-day period during ON and DJFM is consistent with the negative relationship between ALRF and the change in inversion strength among the climate models: a stronger Arctic LRF corresponds to more bottom-heavy warming in the past, i.e. a stronger depletion of the inversion. This explains why the CMIP6/s models end up having a weaker inversion in the present-day period.

During extended winter, the CMIP6/w models are in better agreement with the observations compared to the CMIP6/s subset (Fig. 4b). During ON, the observations lie in between both sub-groups and better match the multi-model mean (not shown). During AMJ both subsets of the models tend to overestimate the inversion strength from the observations. However, the CMIP6/w subset is slightly closer to the observations. During JAS, in turn, both subsets show inversions that are too weak in

https://doi.org/10.5194/acp-2022-836
Preprint. Discussion started: 9 January 2023

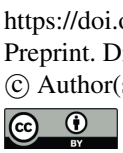

Atmospheric Chemistry and Physics Discussions

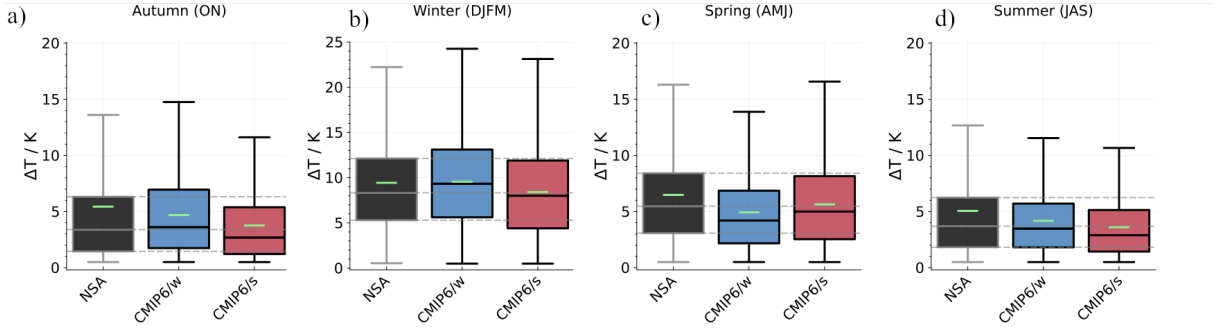

Figure 5. Seasonal inversion strengths ΔT as box plots, obtained from radio soundings at the North Slope of Alaska (NSA) in Utqiaġvik, Alaska, USA, and from the model subsets CMIP6/w and CMIP6/s, respectively. The box plots correspond to Fig. 4b showing the seasonal distribution of ΔT from radio soundings during the MOSAiC expedition. NSA data was collected during 2003–2014, and is compared to co-located 6-hourly model data in the period of 2010–2014. Details on the data processing are given in Section 2.3.

comparison to MOSAiC observations. However, severe data gaps during spring and summer make the interpretation somewhat less reliable.

It is also noteworthy that the atmospheric large-scale circulation during the MOSAiC winter 2019/2020 was characterised by an unusual and long-lasting occurrence of the positive phase of the Arctic Oscillation Index from January to March 2020 (Lawrence et al., 2020; Dethloff et al., 2022). This potentially biases the representativeness of the MOSAiC observations during these months.

3.3 Temperature inversions from radio soundings at Utqiaġvik (NSA)

The regular radiosonde observations at the Utqiaġvik site are complementary to the MOSAiC analysis in that they provide long-term statistics, albeit at one site, and are representative of a different geographical region in the Arctic. We present our results in comparison with the measurements conducted during MOSAiC. Correspondingly, the co-located model data cover the period of 2010–2014 and apply the same CMIP6 models defined in Table 1.

During both ON and DJFM, CMIP6/w models, on average, show a stronger inversion compared to the CMIP6/s subset, and vice versa during AMJ, which is consistent with the findings for the MOSAiC data in Fig. 4. This agreement with the findings from MOSAiC suggests the same explanation also holds true for this longer-term analysis.

The comparison of the observed inversion data with the ones from models shows that the CMIP6/w model subset lies closer to the observations in ON. For the winter case, it is somewhat less clear than for the MOSAiC comparison: The observations lie in between CMIP6/w and CMIP6/s with regard to the 25 and 75-percentile of the data. However, although the CMIP6/w models overestimate the median inversion strength during DJFM, they better agree with previous findings for the NSA site by Kahl (1990). This study reported that during winter (primarily in February) the inversion is stronger (median values of up to 11 K)

https://doi.org/10.5194/acp-2022-836
Preprint. Discussion started: 9 January 2023

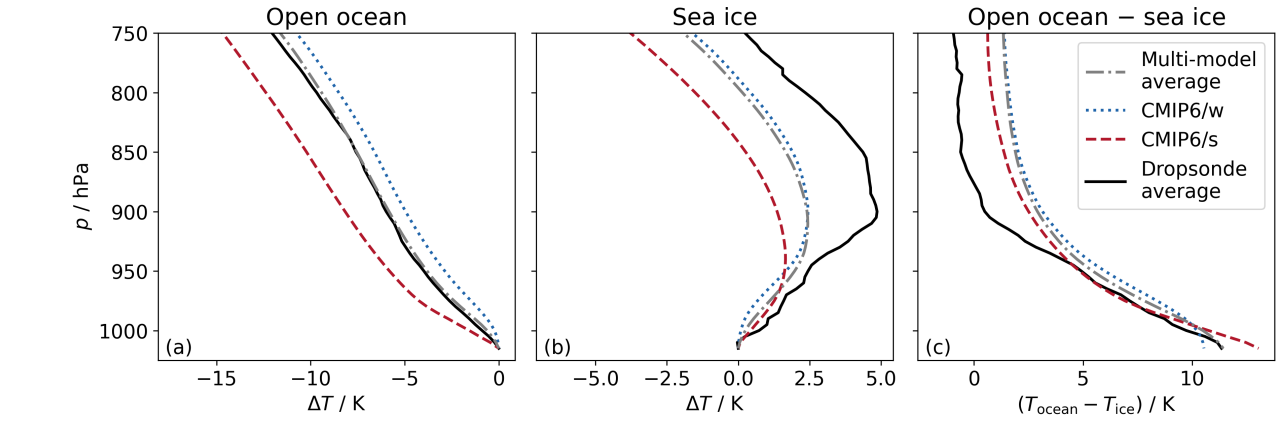

Figure 6. Average profiles of temperature normalized with the temperature at 1015 hPa (ΔT) over a) open ocean, and b) sea ice, respectively. ΔT is obtained from dropsonde launches during aircraft campaigns in the Fram Strait, and the model subsets CMIP6/w and CMIP6/s, just as the model average, respectively. Seasonally, our results are restricted to the month of March. Panel c shows the difference between the temperature profiles over open ocean and sea ice. Dropsonde data was collected during three flight campaigns in 1993, 2013, 2019, and is compared to co-located 6-hourly model data in the period of 2010–2014. Details on the data processing are given in Section 2.4.

compared to our analysis for NSA 2003–2014 (median of 8 K and a mean of 9.5 K). Together with the MOSAiC observations, this hints to the weak-AA models more realistically representing inversion strength during fall and extended winter.

Conversely in spring, the CMIP6/w models underestimate the inversion strength as compared to the observations, while CMIP6/s models fits the observations better. This is in contrast to our MOSAiC results, which suggest that both model groups overestimate the inversion strength at this time of the year. However, due to large data gaps for MOSAiC during this season, caution should be taken while interpreting the results. This makes the NSA comparison more trustworthy. During JAS, the inversion strength is underestimated in all models, a result that is in agreement with the MOSAiC data.

3.4 Temperature profiles from dropsondes in the Fram Strait

In order to assess the mediating effect of the surface type (open ocean or sea ice) on the temperature profile, we make use of dropsonde profiles launched from aircraft. Again, this analysis is complimentary to the results from the MOSAiC and NSA data comparison, embedded in the context of local influences on the Arctic LRF. We thereby apply the same models, but only include data during the end of extended winter (March), as discussed before in Section 2.4. The comparison with co-located CMIP6/w and CMIP6/s model subsets is shown in Fig. 6. Panel a and b show the temperature profiles derived from observations and models over open ocean and sea ice, respectively, which are normalised to the temperature at 1015 hPa. Note that due to a lack of open ocean data in the CNRM-ESM2-1 model (number 25 in Table 1) domain, CMIP6/s only comprises two models.

The mean temperature profiles derived from both models and observations show an almost linear temperature decrease over open ocean, as also expected climatologically (Fig. 2a and b). In contrast, the profile over sea ice shows a near-surface temperature inversion for both observations and model data (again, in agreement with the climatological analysis in Fig. 2).

https://doi.org/10.5194/acp-2022-836
Preprint. Discussion started: 9 January 2023


Atmospheric Chemistry and Physics Discussions

Over ocean, the CMIP6/s subset shows slightly less stable conditions than the CMIP6/w data. Similarly, the CMIP6/w subset simulates a stronger inversion (on average 4.35 K), compared to the CMIP6/s data (on average 3.55 K) over sea ice. The stronger simulated stability in present-day temperature profiles as simulated in the CMIP6/w subset is in agreement with previous results from MOSAiC in the central Arctic, and the NSA site located near the coast during DJFM (and ON). Note that the difference in stability between both subsets weakens when including campaign data from April (not shown). We attribute this to the fact that during AMJ, both MOSAiC and NSA show the opposite, i.e., CMIP6/s models simulate stronger present-day inversions compared to CMIP6/w. This likely leads to less differences between the subsets in the dropsonde data through overlapping signals between March and April. Overall, both model subsets underestimate the inversion strength compared to the observations over sea ice. However, over both open ocean and sea ice, the CMIP6/w subset is closer to the observations, albeit being rather consistent with the multi-model average.

To analyse the impact of sea ice retreat on the temperature profile, Fig. 6c shows the difference in profiles between open-ocean and sea-ice areas. Close to the surface, the temperature difference between ocean and sea ice is larger for the CMIP6/s subset (on average 13.0 K) compared to CMIP6/w (on average 10.5 K). This is mostly due to higher near-surface air temperatures over ocean in the CMIP6/s subset (not shown). However, above 1000 hPa the situation reverses, with a larger surface-type temperature difference for CMIP6/w models. Comparing to the observations, the warming expected through sea ice retreat is slightly better depicted by the CMIP6/w models very close to the surface. However, in higher layers, CMIP6/s models simulate a slightly more realistic temperature difference between profiles over ocean and sea ice (albeit the difference between models subsets is small).

In summary, we conclude that in the context of simulated stability over sea ice and ocean, the dropsonde results representing the month of March are in agreement with the inversion data obtained from the central Arctic during MOSAiC, and at the coast of the NSA site during DJFM. We further show that when switching from sea ice to open ocean, the CMIP6/s models generate a stronger increase in the near-surface air temperature than the CMIP6/w models, but less warming in the higher troposphere. Both implies a stronger contribution to a positive LRF embedded in the processes driving the Arctic LRF: bottom-heavy warming and muted top-heavy warming.

Up to this point, we have presented results that concern local and surface-near Arctic processes and their link to the simulated past AA and Arctic LRF. We now focus on the impact of remote controls, by firstly extending our results shown in Fig. 6c, i.e. the evolution of bottom-heavy and top-heavy warming, and their potential to mediate the vertical warming structure in a model-to-reanalysis comparison.

3.5 The role of advective heating

In this analysis on advective bottom- and top-heavy warming, we focus on the same area of the Fram Strait as in the previous section, and further include the observational site of Utqiaġvik. Bottom-heavy warming conceptually addresses the key feature of the Arctic LRF, i.e. the stronger warming of near-surface air masses compared to aloft. Top-heavy warming on the contrary describes the concept of stronger warming in higher layers of the tropospheric column, compared to the surface. To address these vertically non-uniform warming structures, we analyse changes in the occurrence of those transport pathways that are

https://doi.org/10.5194/acp-2022-836
Preprint. Discussion started: 9 January 2023


Atmospheric Chemistry and Physics Discussions

related to either BHW or THW during extended winter (DJFM). Thereby, we link vertically non-uniform warming structures to circulation patterns. To evaluate the performance of CMIP6 models, we compare CMIP6/w and CMIP6/s model subsets to ERA5 data. The transport pathways are characterised in terms of preferred atmospheric circulation regimes and the warming profiles are described in terms of T2m and T500 anomalies.

The transport pathways over the Fram Strait region (0°–10° E, 77.4°–82° N; see Fig. 3) are characterised by the five distinct circulation regimes over the North Atlantic-Eurasian region (e.g., Crasemann et al., 2017), namely the Scandinavian/Ural blocking regime (SCAN/Ural), the negative phase of North Atlantic Oscillation (NAO-), the dipole pattern regime (DIPOL), the Atlantic trough regime (ATL Trough), and the positive phase of North Atlantic Oscillation (NAO+). The application of the MNLR approach described in Sec. 2.5 reveals a high occurrence probability of the ATL Trough regime for BHW over the Fram Strait for ERA5 (Fig. 7a) as well as for the climate models (not shown). The occurrence of strong THW over the Fram Strait is associated with a high probability of the NAO+ circulation regime (Fig. 7b). For ERA5, Fig. 7c shows that the ATL Trough regime (associated with BHW) occurs more frequently, and the NAO+ regime (associated with THW) less frequently in the present-day period compared to the reference. Although non-significant, both of these changes imply a potentially positive feedback contribution of advection to the Arctic LRF. For the CMIP6/w models, both the ATL Trough and the NAO+ regime occur less frequently in the present-day period with the implication of counteracting effects on the local LRF by advection. On the other hand, for the CMIP6/s models, the ATL Trough regime occurrence increases and the NAO+ regime occurrence decreases in the present-day period. We suggest that the differences in the sign of occurrence changes in the ATL Trough / BHW regime are related to the differences in the strength of ALRF, comparing the two model subsets over the Fram Strait region.

The transport pathways over the Utqiaġvik region (200°–205.9° E, 70.6°–71.8° N; see Fig. 3) are characterised by five distinct circulation regimes over the North Pacific region (e.g., Amini and Straus, 2019), namely the Pacific Trough (PAC Trough), the Arctic High, the Pacific wave train, the Arctic low and the Alaskan ridge regime. By applying the MNLR approach, a high occurrence probability of the Arctic low regime for BHW for ERA5 (Fig. 7d), as well as for the climate models (not shown) has been detected. The occurrence of THW over the Utqiaġvik region is related to a high probability of the PAC Trough regime (Fig. 7e). For ERA5, Fig. 7f shows that the Arctic low regime (associated with BHW) occurs more frequently, and the PAC Trough regime (associated with THW) less frequently in the present-day period. Again, both of these changes in the remote influences, (which at Utqiaġvik, have passed a bootstrap significance test), can positively contribute to the Arctic LRF. For the CMIP6/w models, both the occurrence of the Arctic low regime and the PAC Trough regime increases slightly in the present-day period, with the implication of counteracting effects of advection on the local LRF. For the CMIP6/s models, the Arctic low regime occurrence decreases and the PAC Trough regime occurrence increases in the present-day period, which potentially contributes to a weakening of the positive LRF through advection over the Utqiaġvik region.

In summary, at both sites of the Fram Strait and Utqiaġvik, CMIP6/w and CMIP6/s model subsets differ from each other in terms of their changes in relative frequency of BHW regimes in the present-day period 1985–2014 with respect to 1951–1980: In the Fram-Strait domain, CMIP/w models show a decrease in the relative frequency in BHW, while CMIP6/s models shows an increase. Both have less THW in the present-day period. Thereby, we suggest a negative LRF contribution to CMIP6/w,

https://doi.org/10.5194/acp-2022-836
Preprint. Discussion started: 9 January 2023

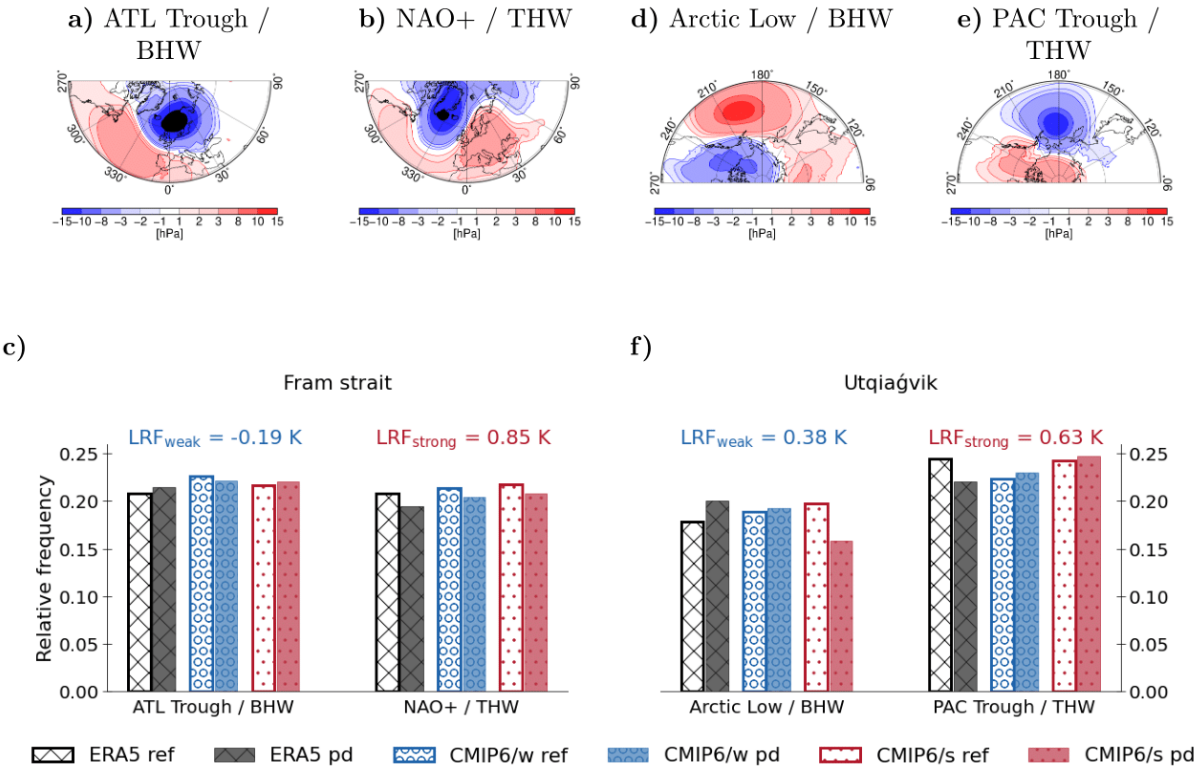

Figure 7. Changes in the relative frequency of circulation regimes associated with either bottom-heavy warming (BHW) or top-heavy warming (THW) for ERA5, and the model subsets CMIP6/w and CMIP6/s, respectively. The left side of the plot refers to the North-Atlantic-Eurasian region (a, b, c), the right side to the North-Pacific region (d, e, f). Upper rows show the circulation regimes, lower rows their frequency of occurrence for reference (ref) and present-day (pd) period, respectively. Seasonally, we focus on the extended winter period DJFM. North-Atlantic-Eurasian region: SLP anomaly patterns of the two circulation regimes which are related to a) strong BHW (Atlantic Trough; ATL Trough) and b) strong THW (NAO+), based on ERA5 daily mean SLP data for 1979–2020. c) Changes in the relative frequency of occurrence between the reference and the present-day period of the respective regimes over the Fram Strait. North Pacific region: d) and e) as in a) and b): SLP anomaly patterns of two circulation regimes which are related to d) strong BHW (Arctic Low) and e) strong THW (Pacific Trough; PAC Trough), based on ERA5 daily mean SLP data for 1979-2020. f) as in to c): Changes in the relative frequency between reference period and present-day period of the respective regimes over Utqiaġvik. The reference and present-day period in ERA5 (CMIP6) is 1979–1999 (1951–1980) and 2000–2020 (1985–2014), respectively. The values above panels c and f give the local LRF for CMIP6/w (LRF_{weak}) and CMIP6/s (LRF_{strong}) over both domains, respectively. We use daily output data for both ERA5 and CMIP6 in this analysis. Details on the data processing are given in Section 2.5

and a positive LRF contribution to CMIP6/s models through the influence of advective BHW in the Fram Strait, respectively. At Utqiaġvik, the situation is reversed. CMIP/w models show an increase in the relative frequency in BHW, while CMIP/s models show a decrease. Both have more THW in the present-day period. Thereby, we suggest a positive LRF contribution

https://doi.org/10.5194/acp-2022-836
Preprint. Discussion started: 9 January 2023

Atmospheric Chemistry and Physics Discussions

to CMIP6/w, and a negative LRF contribution to CMIP6/s models through the influence of advective BHW at Utqiaġvik, respectively. We link these differences between the model subsets at both locations to the magnitude of the co-located LRF (values given in Fig. 7c and f) later on in the discussion.

In terms of their similarities with ERA5 results, the changes in advective BHW/THW show that the CMIP6/s models have a closer resemblance to ERA5 over the Fram Strait. At Utqiaġvik, the ERA5 data show an opposite tendency in the evolution of BHW and THW in comparison with CMIP6/s models. For the CMIP6/w models, only the increase in BHW is consistent with ERA5, albeit less pronounced in the models. Note that by applying a bootstrap test, we determine significant changes only at the site of Utqiaġvik (for changes in BHW/THW in ERA5, and in BHW for CMIP6/s models).

3.6 Pan-Arctic meridional energy transport convergence

In a second step of considering remote controls on the Arctic LRF, we extend the perspective of energy transport to a broader view. Figure 8a depicts the total poleward energy transport convergence within the Arctic boundary during each season for ERA5, CMIP6/w, and CMIP6/s subsets, respectively. The present-day transport accounts for the averaged period of 2000–2014 for both CMIP6 and reanalysis data.

Our results show that during fall, extended winter, and spring the poleward transport convergence is stronger for the CMIP6/s subset. In addition, the transport convergence and AA/ALRF are positively correlated amongst all models with daily diagnostics (Table 1 for reference), during ONDJFM: The inter-model correlation coefficients between energy transport and AA/ALRF are given in the lower part of Fig. 8a. This correlation is particularly strong during ON, with ALRF cor $= 0.76$. During summer, the opposite is the case: CMIP6/w models show a stronger poleward transport convergence, and the transport-AA/ALRF relationship becomes negative (without being statistically significant).

We further calculate the WSD as a measure to define how realistically CMIP6 models reproduce the transport pattern as compared to ERA5 (Section 2.6 for details). The WSDs for both CMIP6/w and CMIP6/s models are shown in Fig. 8b. The lower the magnitude of WSD, the more similar is the CMIP6 simulated transport pattern to ERA5. We equally consider all models in the daily subset to derive inter-model correlation coefficients between WSD and AA/ALRF (values are given in the lower part of Fig. 8b). Our results show that during spring and fall, CMIP6/s models better resemble ERA5 transport patterns compared to CMIP6/w. We find this relationship to be significant, primarily during spring (ALRF cor $= -0.70$, and AA cor $= -0.74$). Furthermore, both CMIP6/s and CMIP6/w subsets perform equally during summer and winter, but more realistically reproduce ERA5 profiles during summer.

In summary, we find that during ONDJFM, models with stronger present-day poleward transport convergence simulate a larger past Arctic LRF and AA, with statistical significance. However, only during ON we find that CMIP6/s models systematically reproduce the ERA5 transport better than CMIP6/w models. The spring season shows no significant correlation for the transport-AA/ALRF correlation, but interestingly, CMIP6/s models more realistically reproduce the ERA5 transport pattern. During summer, the transport-AA/ALRF relationship becomes negative (but without significance), with all models in our CMIP6/w/s subset realistically reproducing the ERA5 transport profile. We further elaborate on the connection between the Pan-Arctic transport perspective and the Arctic LRF and AA in the discussion.

https://doi.org/10.5194/acp-2022-836
Preprint. Discussion started: 9 January 2023

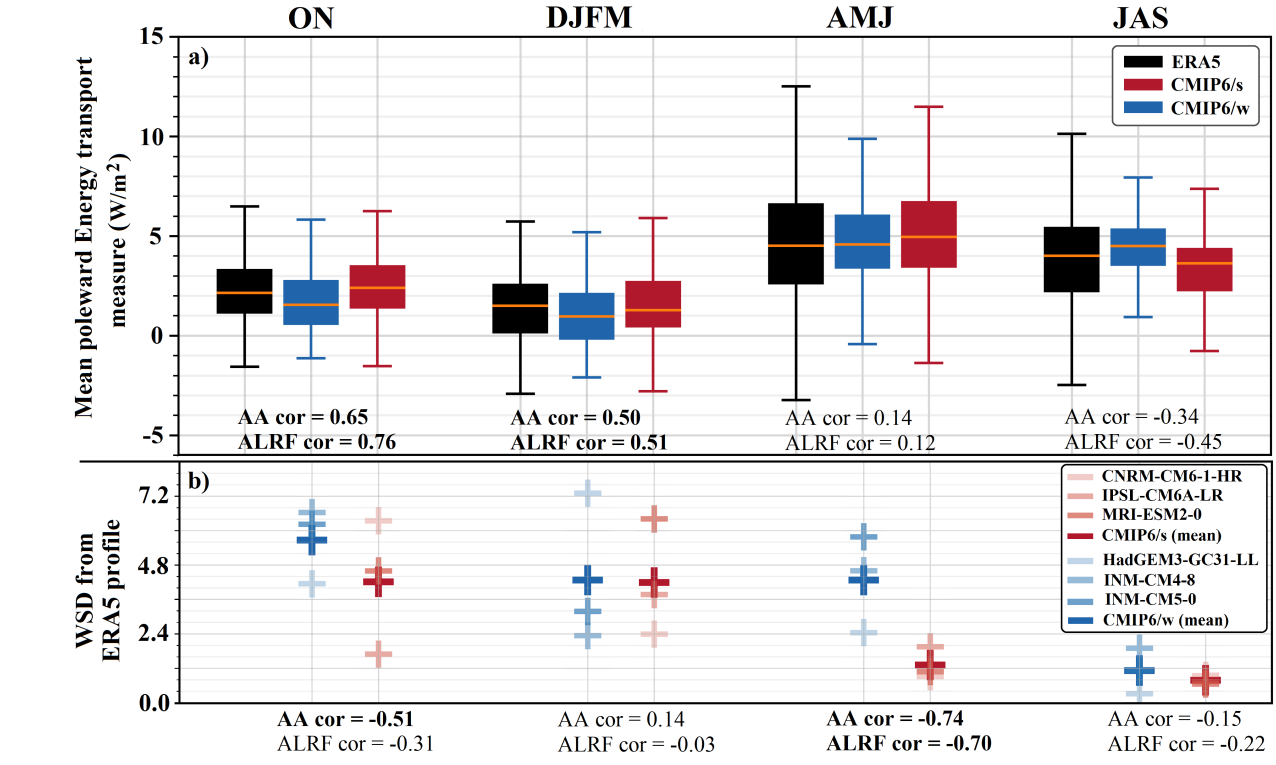

Figure 8. a) Seasonal Pan-Arctic energy transport convergence north of 66° N, obtained from ERA5, and the model subsets CMIP6/w and CMIP6/s, respectively, during 2000–2014. The seasonal inter-model correlation coefficients between transport and historical AA / ALRF (including all models in Table 1 with daily resolution) are given in the lower part of each panel. b) Mean Wasserstein distance (WSD) between ERA5 transport patterns and the corresponding CMIP6 patterns for CMIP6/w and CMIP6/s subsets, respectively. The WSD for individual CMIP6/w and CMIP6/s models are shown by transparent crosses. The seasonal inter-model correlation coefficients between WSD and AA / ALRF are given in the lower part of each panel. Correlation coefficients that are statistically significant are marked in bold. We use daily output data for both ERA5 and CMIP6 in this analysis. Details on the data processing are given in Section 2.6.

3.7 Pan-Arctic outgoing long-wave radiation at the TOA

As introduced earlier, the global LRF builds on either limited atmospheric cooling in the long-wave spectrum (as in the Arctic), or an intensification of this process (i.e. a reduced Greenhouse effect). Thereby, the LRF (amongst other feedbacks and forcings) mediates changes in TOA energy budget in the long-wave radiation spectrum. In our final step, we investigate changes in the outgoing long-wave radiation at the TOA during past decades. Within the scope of the TOA energy budget, we seek to constrain the overall LRF in the Arctic by a model-to-satellite data comparison, covering the period of 1982–2014 (from the beginning of the satellite record to the end of the CMIP6 simulations).

Figure 9 depicts an overall increases in OLR within the period of interest which is consistent with atmospheric warming. The CMIP6/s subset shows a stronger increase in OLR compared to CMIP6/w which coincides with a notoriously stronger warming

https://doi.org/10.5194/acp-2022-836
Preprint. Discussion started: 9 January 2023

Atmospheric Chemistry and Physics Discussions

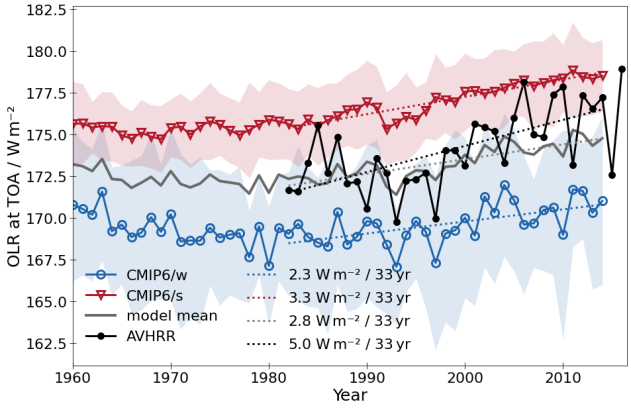

Figure 9. Time series of net outgoing long-wave radiation at TOA (all-sky) for AHVRR satellite retrievals, and the model subsets CMIP6/w and CMIP6/s, respectively. Trends are derived for both satellite observations and model subsets as linear fit between 1982 and 2014, from the beginning of the satellite record to the end of the historical CMIP6 simulations. The fluxes are averaged over the Arctic area north of 66° N, and account for the extended winter period DJFM. For the comparison, we use the collection of monthly-mean model diagnostics. Details on the data processing are given in Section 2.7.

in the CMIP6/s simulations (not shown). However, we cannot detect a signal of the stronger past Arctic LRF in the CMIP6/s subset here, as this would imply less OLR at the TOA, compared to the CMIP6/w simulations (again, the LRF increases the local Greenhouse effect in the Arctic). Thereby, the stronger warming effect overshadows the feedback signal.

Comparing model data and observations, the satellite-based time series is in between both model simulations, close to the model average (not shown). However, the observations show a stronger increase in OLR (5.0 $\mathrm{Wm^{-2}}$) over the 33-year period of 1982–2014, compared to both CMIP6/w and CMIP6/s subsets (with an increase of 2.3 $\mathrm{Wm^{-2}}$ and 3.3 $\mathrm{Wm^{-2}}$, respectively). Overall, the CMIP6/s subset is closer to the observations in terms of trends in the time period of 1982–2014, but still underestimates the increase in OLR. We discuss this more in depth later on.

Up to this point, we compared key features of the Arctic LRF and AA in the current climate to co-located model simulations with both weak and strong simulated ALRF and AA in the past. Our model-to-observation (model-to-reanalysis) comparisons covered the key aspects of Arctic temperature inversions, sea ice retreat, advection of energy transport, and the link between LRF and changes in the TOA energy budget with warming. On the other hand, processes at turbulence- and cloud-resolving scales are largely underrepresented in the literature covering the Arctic LRF. In our final step, we show the potential of these processes to impact the evolution of the Arctic temperature profile. We thereby link to our results in Fig. 2 which briefly motivated the role of clouds in the evolution of the Arctic LRF in a purely CMIP6-based analysis. The next section deepens this analysis in the scope of a local energy budget perspective in large-eddy simulations covering the MOSAiC drift. We treat this section separately from the constraint approach, and thereby drop the comparison to CMIP6 simulations in an outlook perspective.

https://doi.org/10.5194/acp-2022-836
Preprint. Discussion started: 9 January 2023

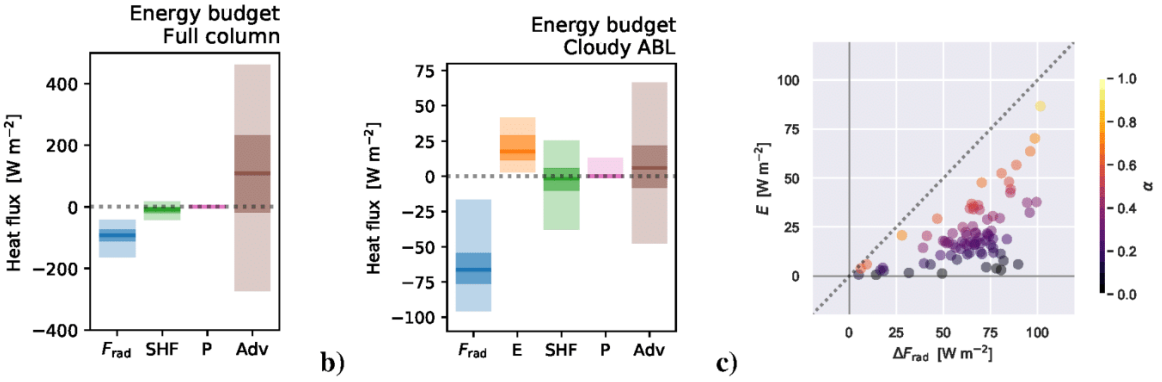

Figure 10. LES results for the MOSAiC drift. a) Drift-average heat budget of the full atmospheric column. b) Conditionally averaged ABL heat budget for all days with a non-zero liquid water path (83 out of 300 simulated days). Budget terms include net radiative heating (F_{rad}), top entrainment heat flux (E), surface sensible heat flux (SHF), surface precipitation in any form (P), and vertically integrated large-scale advection (Adv). Each term is shown as a distribution, with the median (thick line), interquartile range (dark shaded) and 9-95 percentile range (light shaded). c) Scatter plot of daily average long-wave cooling across the liquid cloud layer versus the entrainment heat flux at the atmospheric boundary layer inversion. Coloring represents the entrainment efficiency α, as defined in the text. Details on the data processing are given in Section 2.8.

3.8 The role of advection, clouds and entrainment in large-eddy simulations (LES)

To gain further insight in the role of clouds and boundary-layer dynamics, we now investigate the Arctic energy budget in more detail, using output data from year-long LES covering the MOSAiC drift. The results are shown in Fig. 10.

Averaged over all 300 daily simulations we find that the full column heat budget is approximately in radiative-advective equilibrium (RAE; Fig. 10a). Even if only a certain number of weather situations were sampled during the drift, and even if the scatter in particular in the advective heating remains large, this confirms what is expected for the large-scale energy budget of the ice-covered Arctic: In particular, the surface flux (SHF) and precipitation (P; representing net condensation and freezing in the column) are negligible compared to the radiative cooling (F_{rad}) and vertically integrated advective heating (Adv).

The situation is rather different, though, when i) only analysing cases with low level liquid cloud mass, and ii) considering the heat budget for the Atmospheric Boundary Layer (ABL). For the whole drift about 1 out of 3 days features low level liquid clouds. This frequency of occurrence is roughly consistent with the findings of Bennartz et al. (2013), and is an expression of the resilience of mixed phase clouds at high latitudes (Morrison et al., 2012). In contrast to the full column, the ABL heat budget shows an imbalance in which the radiative cooling dominates (Fig. 10b). On average, this leads to a gradual cooling of the ABL in cloudy cases, which likely expresses the ongoing transformation of warm and moist air masses in which these clouds are embedded (Pithan and Mauritsen, 2014; Pithan et al., 2018).

An intriguing result in the context of the LRF is the significant role played by entrainment at the top of the ABL, here defined as the height of the strongest gradient in liquid water potential temperature (θ_l) in the lowest 5 km. In these cloudy

https://doi.org/10.5194/acp-2022-836
Preprint. Discussion started: 9 January 2023


Atmospheric Chemistry and Physics Discussions

cases, in addition to the weak advective heating, the warming of the ABL due to the entrainment flux (E) is significant, while sensible and latent heat flux are again negligible as was the case in all-sky conditions (Fig. 10b). The entrainment heating ($E = \epsilon_t \, \Delta\theta_l$) depends on the ABL-top entrainment rate (ϵ_t) and the temperature jump across the inversion ($\Delta\theta_l$), an expression of local (elevated) inversion strength. Entrainment warming can only counteract the radiative cooling partially, an effect which is investigated in further detail in Fig. 10c. The impact on the ABL heat budget is expressed by the entrainment efficiency (α), defined as the ratio of entrainment warming to the radiative cooling (Stevens et al., 2005):

$$\alpha = \frac{\epsilon_t \, \Delta\theta_l}{|F_{\mathrm{rad}}|} \, . \tag{4}$$

We find, on the basis of these year-long LES results for the MOSAiC drift, that for mixed phase Arctic clouds this ratio is about 1/3, implying that entrainment warming is never able to fully balance the radiative cooling. However, it still significantly counteracts the gradual cooling of warm and moist air masses that enter the Arctic system. In this process, the main role of inversion strength is to determine the entrainment warming. As a result, it modulates the transformation of such warm cloudy air masses, to the effect that it keeps them warm for longer. This in turn affects the LRF, in particular in ice-covered areas over which such cloudy air masses travel.

4 Discussion

In the present study, we compile a sizeable amount of observations in order to constrain the Arctic LRF and the Arctic amplification of climate change during past decades. We concentrate on the ALRF and AA for the historical past, defined here as the time period of 1951–2014. For our process-oriented constraints we make use of the hypothesis that the Arctic LRF is related to the lack of mixing (e.g., Manabe and Wetherald, 1975) and meridional heat transport within the Arctic region. An analysis of the CMIP6 multi-model ensemble demonstrates that ALRF and AA are linearily connected, and that there is a large spread in both quantities amongst the climate models. This enables us to apply a constraint approach by falsifying subsets of CMIP6 models with either weak or strong simulated ALRF/AA (CMIP6/w or CMIP6/s, respectively), based on observations. Thereby, we link key processes of the current climate to historical climate simulations.

Our results firstly show that models with stronger positive ALRF contribute more to AA both through locally enhancing global warming in the Arctic, and cooling the tropics, which does not necessarily reflect in the inter-model spread of global warming. We secondly present model-to-observation (reanalysis) comparisons covering key aspects of the current Arctic climate system. Previous literature, since the earliest global dynamical simulations of climate change, demonstrate that stable stratification is a necessary condition for a positive LRF in the Arctic (Manabe and Wetherald, 1975). This leads to the hypothesis that the Arctic LRF inter-model spread is correlated to the change in inversion strength, associated with bottom-heavy warming (Boeke et al., 2021; Feldl et al., 2020). Another hypothesis suggests that stronger intial stratification produces a more positive feedback (Boeke et al., 2021; Lauer et al., 2020), without there being a consensus among scientists. Here, we look at present-day surface-based temperature inversion data in the scope of a model-to-observation comparison. We use two data sets of radiosondes launched during the MOSAiC expedition in the central Arctic, and from the permanent ARM site at Utqiaġvik

https://doi.org/10.5194/acp-2022-836
Preprint. Discussion started: 9 January 2023


Atmospheric Chemistry and Physics Discussions

(NSA). Using dropsonde observations from research aircraft during several boreal-springtime campaigns, we quantify the contrast in temperature profiles over sea ice and open ocean in the Fram Strait. We aim to constrain the impact of sea ice retreat, which is widely considered as a strong source of bottom-heavy warming.

In spite of their spatio-temporal differences in data acquisition, we find distinct similarities in the individual comparisons of MOSAiC, NSA, and dropsonde data to CMIP6: Our results confirm that during fall and extended winter (ONDJFM), models that simulate a weaker AA/ALRF in the past, have stronger inversions in the present. We argue that during fall and winter, the key feature of the positive Arctic LRF, bottom-heavy warming, has led to a stronger depletion of the surface-based temperature inversion in the models with stronger AA/ALRF since 1951–1980. Based on the CMIP6 comparison to dropsonde data, we show that even though the CMIP6/s models show weaker present-day inversions (consistent with MOSAiC and NSA), sea ice melt remains an important process to mediate a stronger bottom-heavy warming, and by extension LRF in future scenarios, compared to CMIP6/w models. These results suggest an overall more realistic depiction of surface-near, local Arctic processes by models with weak simulated AA/ALRF in the past during ONDJFM, where the magnitude to AA and ALRF is strong.

On the other hand, not only local processes have the potential to mediate the ALRF, but also remote influences by advection of poleward energy transport. Firstly, we consider the impact of advective bottom- and top-heavy warming on the LRF which are connected to changes in typical circulation regimes. The hypothesis is that an increased frequency of occurrence of weather situations favouring BHW imposes a positive contribution on the LRF. In turn, more frequent events of THW aids long-wave cooling in higher layers, thereby weakening the positive LRF. We focus on the period of extended winter (DJFM) in our analysis, and locally, on the observational sites of Utqiaġvik and the Fram Strait. At the two measuring sites, CMIP6/w and CMIP6/s models differ from each other in terms of their change in relative frequency of BHW regimes ongoing from 1951. We suggest a link between the change in advective BHW and LRF at site: Our data show that in the Fram Strait, the difference in LRF between CMIP6/w (-0.19 K) and CMIP6/s (0.85 K) is larger (1.04 K) compared to Utqiaġvik, where the difference in LRF between CMIP6/w (0.38 K) and CMIP6/s (0.63 K) is smaller (0.25 K) by a factor 4. We relate this to an increase (decrease) in BHW in CMIP6/s (CMIP6/w) in the Fram Strait region, where we hence expect an even bigger spread in local LRF between both model subsets, and a decrease (increase) in BHW in CMIP6/s (CMIP6/w) at the site in Utqiaġvik, where we hence expect a reduction in the spread in local LRF between both model subsets. In short, advective BHW increases the climatological spread between CMIP6/w and CMIP6/s simulated LRF in the Fram Strait, and decreases it at Utqiaġvik. Although we cannot exclude that these differences are mediated by changes in the local factors (e.g., sea ice reduction) between the two simulations, our results hint to a signature of advective influences mediating the spatial pattern of the Arctic LRF. In the Fram Strait region, we find that the increasing frequency of occurrence of transport pathways related to BHW in the CMIP6/s subset coincide with the reanalysis result. However, in the Utqiaġvik region, no conclusive result is found in this regard.

While we present our previous results as a detailed analysis of the vertically resolved temperature change, we secondly extent this perspective to speculate on the coupling between Pan-Arctic energy transport (convergence) and past AA/ARLF. Our results show that during ONDJFM, a stronger present-day transport convergence within the Arctic boundary is statistically related to a stronger annual-mean ALRF/AA in the past. It is noteworthy that we derive the transport as a residual of the energy budget. Hence, we present the total, columnar energy transport convergence without distinguishing dry static and

https://doi.org/10.5194/acp-2022-836
Preprint. Discussion started: 9 January 2023


Atmospheric Chemistry and Physics Discussions

latent transport components. Previous studies have identified the poleward transport of moisture as a crucial process adding to amplified surface warming in the Arctic through the increase in downward long-wave radiation (e.g., Kapsch et al., 2013; Gong et al., 2017; Graversen and Langen, 2019). We thereby suggest that the positive relationship between poleward transport convergence within the Arctic boundary and prior AA during fall and winter is an effect of the moisture component of transport: A stronger accumulation of latent energy in the Arctic in CMIP6/s models has contributed to a stronger amplification of surface warming, and has ultimately led to higher magnitudes in the present-day transport term. We further show that the CMIP6/s models overall resemble ERA5 transport patterns more realistically, primarily during the shoulder seasons. Considering the link between transport and ALRF, Feldl et al. (2020) show that in climate models a larger increase in poleward atmospheric energy transport is associated with a smaller positive ALRF, which contradicts our results. However, in our analysis, local and remote processes are intertwined: For instance, stronger transport can aid top-heavy warming in the atmosphere and thereby negatively contribute to the LRF (as suggested by Feldl et al., 2020). In contrast, stronger transport, primarily intrusions of water vapour into the Arctic during winter, can aid sea-ice melt events (Woods et al., 2013; Yang and Magnusdottir, 2017), which is largely considered a positive contribution to the Arctic LRF.

Ultimately, trends in outgoing long-wave radiation at the TOA finalise the constraints of AA and ALRF in the past within an energy budget perspective that incorporates all processes, local and remote. Our results underline that it is somewhat ambiguous to constrain the historical AA and Arctic LRF as either weak or strong based upon our model classification. However, trends in the 33 years of available satellite observations suggest that historical AA and ALRF are slightly more realistically resembled by strong-AA models. The fact that our proxy of the overall LRF lies between both simulation categories, somewhat reflects that both local and remote influences do not reveal a consensus: The former constraint shows that local influences are rather resembled by CMIP6/w models, whereas remote influences are better represented by CMIP6/s models, where a comparison was appropriate.

To motivate a deeper perspective on clouds, boundary layer dynamics, and advective heating at process level, we conduct a large sample of small-domain daily LES complementing the MOSAiC full drift. Averaged over all cases, radiative cooling of the full atmospheric column is balanced by advective heating (RAE). However, for liquid-bearing cloudy boundary layers the entrainment heating of the boundary layer is significant, even more important than horizontal advection, despite only modest efficiency in counteracting the radiative cooling. This links to Fig. 2c, which implies a negative contribution of clouds to the LRF in the lower ABL (extending up to 850 hPa), but a positive contribution in higher layers. We draw two conclusions from this result: Firstly, entrainment heating represents a significant column-internal redistribution of heat, which impacts the lapse-rate over sea ice. Secondly, liquid-bearing cloudy boundary layers are not in strict RAE but are closer to RCE due to the significance of top-down convective heating through entrainment. However, a full equilibrium is not reached, indicating that these liquid-bearing low level air masses are still in the process of cooling. How these low level processes in effect contribute to AA requires further research, for example by conducting LES for perturbed climate conditions.

Beyond the processes analysed in the present study, also the rate at which sea ice melted in the study period plays a large role for simulated AA and LRF. However, we do not find a strong relation between skill in simulating sea ice and its decline, and the magnitude of AA within a model. CMIP6 models that are identified as capable of simulating a realistic amount of sea-ice

https://doi.org/10.5194/acp-2022-836
Preprint. Discussion started: 9 January 2023


Atmospheric Chemistry and Physics Discussions

loss together with a plausible change in global mean temperature over time (1979–2014; Notz and the SIMIP Community, 2020) span across our collection of models (acronyms marked in bolt in Table 1).

5 Conclusions

In the scope of our main hypotheses formulated in point 1–3 of the introduction, we conclude the following:

1. Our data sets in boreal fall and winter show that local processes mediating the lower thermodynamic structure of the atmosphere are more realistically depicted in climate models with weak simulated ALRF/AA in the past. These models in particular simulate a stronger present-day inversion through less depletion in the past, and generate a smaller low-level warming through sea ice retreat. The latter suggests a smaller potential to generate a positive LRF through the process of sea ice retreat, i.e., weak-AA/LRF models remain weak-AA/LRF models in future scenarios in this context.

2. The analysis of both vertically resolved atmospheric advection, and columnar meridional energy transport leads to the opposite conclusion: remote influences that can further mediate the warming structure in the free troposphere are more realistically represented by climate models with strong simulated ALRF/AA in the past (where the comparison is legitimate). In particular, models with stronger past ALRF/AA systematically simulate a stronger present-day energy transport convergence in the Arctic during boreal fall and winter, which is consistent with reanalyses. For these simulations, we further find links between changes in transport pathways and vertical warming structures that favor a positive LRF.

3. We point out that in some cases of our analysis, no conclusive result are found, for instance when evaluating the performance of climate models to reproduce tendencies in BHW at Utqiaġvik. LES results point to the cloudy conditions for a possible explanation. In cloudy cases, the vertical mixing becomes an important heating term for the atmospheric boundary layer, and it is plausible that the general circulation models are not well able to adequately simulate this contribution. In conclusion, we want to motivate the perspective on the role of clouds and boundary layer dynamics, and their representation in climate models in the framework of local energy budget and vertical heat distribution.

Code availability. The LES code (DALES) used in this study is open access and available on GitHub at *https://github.com/dalesteam/dales*. The current version of DALES (*https://doi.org/10.5281/zenodo.5642477* : dales 4.3 with extension for mixed-phase microphysics) is available on github as *https://github.com/jchylik/dales/releases/tag/dales4.3sb3cgn*.

Data availability. The CMIP6 data are available from the Earth System Grid Federation (ESGF) system: https://esgf-node.ipsl.upmc.fr/projects/esgf-ipsl/, ESGF, 2022 (Eyring et al., 2016). Data from radiosondes launched during the MOSAiC expedition can be downloaded from PANGEA: https://doi.pangaea.de/10.1594/PANGAEA.928656 (Maturilli et al., 2021). NSA radiosonde data are available at the DOE ARM data repository https://adc.arm.gov (Jensen et al., 1998). Dropsonde data from the three different aircraft campaigns considered in our study can be downloaded from the PANGAEA repository: Lüpkes and Schlünzen (1996); Lüpkes et al. (2021); Becker et al. (2020). ERA5

https://doi.org/10.5194/acp-2022-836
Preprint. Discussion started: 9 January 2023

data can be downloaded from the ECMWF data catalogue: https://apps.ecmwf.int/data-catalogues/era5/?class=ea (Hersbach et al., 2020). AVHRR satellite data are available at the DWD website: https://doi.org/10.5676/DWD/ESA_Cloud_cci/AVHRR-PM/V003.

Author contributions. The study was conceived by O.L. and J.Q. with contributions by all authors. O.L. performed the CMIP6 model analyses and many of the model-to-data comparisons. C.S. contributed the feedback analysis tools and advised on their application and interpretation. B.V. and O.L. analysed the MOSAiC radiosondes vs. CMIP models with substantial help by M.S. and S.D. The Utqiaġvik analysis was from P.S.G., F.B. and H.K.-L. together with O.L.. S.B., A.E. and M.W. contributed the ropsonde analysis together with O.L.. The transport patterns were analysed by D.H. with input from O.L.. The energy transport is contributed by S.M. and C.J. with support by O.L.. R.N., J.C. and N.S. performed and analysed the LES; M.V., L.L. and K.V. analysed the satellite retrievals. G.S. advised on the role of sea ice. All authors contributed to the manuscript writing.

Competing interests. The authors declare no competing interests.

Acknowledgements. We gratefully acknowledge the funding by the Deutsche Forschungsgemeinschaft (DFG, German Research Foundation) – Projektnummer 268020496 – TRR 172, within the Transregional Collaborative Research Center "ArctiC Amplification: Climate Relevant Atmospheric and SurfaCe Processes, and Feedback Mechanisms (AC)^3".

https://doi.org/10.5194/acp-2022-836
Preprint. Discussion started: 9 January 2023

Atmospheric Chemistry and Physics Discussions

References

Amini, S. and Straus, D. M.: Control of storminess over the Pacific and North America by circulation regimes, Climate Dynamics, 52, 4749–4770, https://doi.org/10.1007/s00382-018-4409-7, 2019.

Becker, S., Ehrlich, A., Stapf, J., Lüpkes, C., Mech, M., Crewell, S., and Wendisch, M.: Meteorological measurements by dropsondes released from POLAR 5 during AFLUX 2019, PANGAEA - Data Publisher for Earth & Environmental Science [data set], https://doi.org/10.1594/PANGAEA.921996, 2020.

Bennartz, R., Shupe, M. D., Turner, D. D., Walden, V. P., Steffen, K., Cox, C. J., Kulie, M. S., Miller, N. B., and Pettersen, C.: July 2012 Greenland melt extent enhanced by low-level liquid clouds, Nature, 496, 83–86, https://doi.org/10.1038/nature12002, 2013.

Bentsen, M., Oliviè, D. J. L., Seland, y., Toniazzo, T., Gjermundsen, A., Graff, L. S., Debernard, J. B., Gupta, A. K., He, Y., Kirkevåg, A., Schwinger, J., Tjiputra, J., Aas, K. S., Bethke, I., Fan, Y., Griesfeller, J., Grini, A., Guo, C., Ilicak, M., Karset, I. H. H., Landgren, O. A., Liakka, J., Moseid, K. O., Nummelin, A., Spensberger, C., Tang, H., Zhang, Z., Heinze, C., Iversen, T., and Schulz, M.: NCC NorESM2-MM model output prepared for CMIP6 CMIP, Earth System Grid Federation [data set], https://doi.org/10.22033/ESGF/CMIP6.506, 2019.

Block, K., Schneider, F. A., Mülmenstädt, J., Salzmann, M., and Quaas, J.: Climate models disagree on the sign of total radiative feedback in the Arctic, Tellus A, 72, 1–14, https://doi.org/10.1080/16000870.2019.1696139, 2020.

Boeke, R. C., Taylor, P. C., and Sejas, S. A.: On the Nature of the Arctic's Positive Lapse-Rate Feedback, Geophysical Research Letters, 48, e2020GL091 109, https://doi.org/https://doi.org/10.1029/2020GL091109, 2021.

Boucher, O., Denvil, S., Levavasseur, G., Cozic, A., Caubel, A., Foujols, M.-A., Meurdesoif, Y., Cadule, P., Devilliers, M., Ghattas, J., Lebas, N., Lurton, T., Mellul, L., Musat, I., Mignot, J., and Cheruy, F.: IPSL IPSL-CM6A-LR model output prepared for CMIP6 CMIP, Earth System Grid Federation [data set], https://doi.org/10.22033/ESGF/CMIP6.1534, 2018.

Cao, J. and Wang, B.: NUIST NESMv3 model output prepared for CMIP6 CMIP, Earth System Grid Federation [data set], https://doi.org/10.22033/ESGF/CMIP6.2021, 2019.

Cox, C., Gallagher, M., Shupe, M., Persson, O., Solomon, A., Blomquist, B., Brooks, I., Costa, D., Gottas, D., Hutchings, J., et al.: 10-meter (m) meteorological flux tower measurements (Level 1 Raw), Multidisciplinary drifting observatory for the study of arctic climate (MOSAiC), central Arctic, October 2019–September 2020, Arctic Data Center [data set], https://doi.org/10.18739/A2VM42Z5F, 2021.

Crasemann, B., Handorf, D., Jaiser, R., Dethloff, K., Nakamura, T., Ukita, J., and Yamazaki, K.: Can preferred atmospheric circulation patterns over the North-Atlantic-Eurasian region be associated with arctic sea ice loss?, Polar Science, 14, 9–20, https://doi.org/10.1016/j.polar.2017.09.002, 2017.

Creamean, J.: Size-resolved ice nucleating particle (INP) concentrations from the MOSAiC campaign, ARM Research Facility [data set], https://doi.org/10.5439/1798162, 2019.

Crook, J. A., Forster, P. M., and Stuber, N.: Spatial patterns of modeled climate feedback and contributions to temperature response and polar amplification, Journal of Climate, 24, 3575–3592, 2011.

Danabasoglu, G.: NCAR CESM2-FV2 model output prepared for CMIP6 CMIP, Earth System Grid Federation [data set], https://doi.org/10.22033/ESGF/CMIP6.11281, 2019a.

Danabasoglu, G.: NCAR CESM2-WACCM-FV2 model output prepared for CMIP6 CMIP, Earth System Grid Federation [data set], https://doi.org/10.22033/ESGF/CMIP6.11282, 2019b.

Danabasoglu, G.: NCAR CESM2-WACCM model output prepared for CMIP6 CMIP, Earth System Grid Federation [data set], https://doi.org/10.22033/ESGF/CMIP6.10024, 2019c.

https://doi.org/10.5194/acp-2022-836
Preprint. Discussion started: 9 January 2023

Danabasoglu, G.: NCAR CESM2 model output prepared for CMIP6 CMIP, Earth System Grid Federation [data set], https://doi.org/10.22033/ESGF/CMIP6.2185, 2019d.

Danek, C., Shi, X., Stepanek, C., Yang, H., Barbi, D., Hegewald, J., and Lohmann, G.: AWI AWI-ESM1.1LR model output prepared for CMIP6 CMIP, Earth System Grid Federation [data set], https://doi.org/10.22033/ESGF/CMIP6.9301, 2020.

Dawson, A. and Palmer, T. N.: Simulating weather regimes: Impact of model resolution and stochastic parameterization, Climate Dynamics, 44, 2177–2193, https://doi.org/10.1007/s00382-014-2238-x, 2015.

Dethloff, K., Maslowski, W., Hendricks, S., Lee, Y., Goessling, H. F., Krumpen, T., Haas, C., Handorf, D., Ricker, R., Bessonov, V., Cassano, J. J., Kinney, J. C., Osinski, R., Rex, M., Rinke, A., Sokolova, J., and Sommerfeld, A.: Arctic sea ice anomalies during the MOSAiC winter 2019/20, The Cryosphere, 16, 981–1005, https://doi.org/10.5194/tc-16-981-2022, 2022.

Detring, C., Müller, A., Schielicke, L., Névir, P., and Rust, H. W.: Occurrence and transition probabilities of omega and high-over-low blocking in the Euro-Atlantic region, Weather and Climate Dynamics, 2, 927–952, https://doi.org/10.5194/wcd-2-927-2021, 2021.

Eyring, V., Bony, S., Meehl, G. A., Senior, C. A., Stevens, B., Stouffer, R. J., and Taylor, K. E.: Overview of the Coupled Model Intercomparison Project Phase 6 (CMIP6) experimental design and organization, Geoscientific Model Development, 9, 1937–1958, https://doi.org/10.5194/gmd-9-1937-2016, 2016.

Fabiano, F., Meccia, V. L., Davini, P., Ghinassi, P., and Corti, S.: A regime view of future atmospheric circulation changes in northern mid-latitudes, Wea. Climate Dyn., 2, 163–180, https://doi.org/10.5194/wcd-2-163-2021, 2021.

Feldl, N. and Roe, G.: Four perspectives on climate feedbacks, Geophysical Research Letters, 40, 4007–4011, 2013.

Feldl, N., Bordoni, S., and Merlis, T. M.: Coupled High-Latitude Climate Feedbacks and Their Impact on Atmospheric Heat Transport, Journal of Climate, 30, 189 – 201, https://doi.org/10.1175/JCLI-D-16-0324.1, 2017.

Feldl, N., Po-Chedley, S., Singh, H. K., Hay, S., and Kushner, P. J.: Sea ice and atmospheric circulation shape the high-latitude lapse rate feedback, NPJ climate and atmospheric science, 3, 1–9, 2020.

Gong, T., Feldstein, S., and Lee, S.: The role of downward infrared radiation in the recent Arctic winter warming trend, Journal of Climate, 30, 4937–4949, 2017.

Goosse, H., Kay, J. E., Armour, K. C., Bodas-Salcedo, A., Chepfer, H., Docquier, D., Jonko, A., Kushner, P. J., Lecomte, O., Massonnet, F., et al.: Quantifying climate feedbacks in polar regions, Nature communications, 9, 1–13, 2018.

Graversen, R. G. and Langen, P. L.: On the Role of the Atmospheric Energy Transport in 2× CO 2–Induced Polar Amplification in CESM1, Journal of Climate, 32, 3941–3956, 2019.

Guo, H., John, J. G., Blanton, C., McHugh, C., Nikonov, S., Radhakrishnan, A., Rand, K., Zadeh, N. T., Balaji, V., Durachta, J., Dupuis, C., Menzel, R., Robinson, T., Underwood, S., Vahlenkamp, H., Bushuk, M., Dunne, K. A., Dussin, R., Gauthier, P. P., Ginoux, P., Griffies, S. M., Hallberg, R., Harrison, M., Hurlin, W., Lin, P., Malyshev, S., Naik, V., Paulot, F., Paynter, D. J., Ploshay, J., Reichl, B. G., Schwarzkopf, D. M., Seman, C. J., Shao, A., Silvers, L., Wyman, B., Yan, X., Zeng, Y., Adcroft, A., Dunne, J. P., Held, I. M., Krasting, J. P., Horowitz, L. W., Milly, P., Shevliakova, E., Winton, M., Zhao, M., and Zhang, R.: NOAA-GFDL GFDL-CM4 model output, Earth System Grid Federation [data set], https://doi.org/10.22033/ESGF/CMIP6.1402, 2018.

Hahn, L. C., Armour, K. C., Zelinka, M. D., Bitz, C. M., and Donohoe, A.: Contributions to polar amplification in CMIP5 and CMIP6 models, Frontiers in Earth Science, p. 725, 2021.

Hajima, T., Abe, M., Arakawa, O., Suzuki, T., Komuro, Y., Ogura, T., Ogochi, K., Watanabe, M., Yamamoto, A., Tatebe, H., Noguchi, M. A., Ohgaito, R., Ito, A., Yamazaki, D., Ito, A., Takata, K., Watanabe, S., Kawamiya, M., and Tachiiri, K.: MIROC MIROC-ES2L model output prepared for CMIP6 CMIP, Earth System Grid Federation [data set], https://doi.org/10.22033/ESGF/CMIP6.902, 2019.

https://doi.org/10.5194/acp-2022-836
Preprint. Discussion started: 9 January 2023

Hegyi, B. M. and Deng, Y.: Dynamical and thermodynamical impacts of high-and low-frequency atmospheric eddies on the initial melt of Arctic sea ice, Journal of Climate, 30, 865–883, https://doi.org/10.1175/JCLI-D-15-0366.1, 2017.

Hegyi, B. M. and Taylor, P. C.: The unprecedented 2016–2017 Arctic sea ice growth season: The crucial role of atmospheric rivers and longwave fluxes, Geophysical research letters, 45, 5204–5212, https://doi.org/10.1029/2017GL076717, 2018.

Henderson, D. S., L'Ecuyer, T., Stephens, G., Partain, P., and Sekiguchi, M.: A Multisensor Perspective on the Radiative Impacts of Clouds and Aerosols, Journal of Applied Meteorology and Climatology, 52, 853 – 871, https://doi.org/10.1175/JAMC-D-12-025.1, 2013.

Hersbach, H., Bell, B., Berrisford, P., Hirahara, S., Horányi, A., Muñoz-Sabater, J., Nicolas, J., Peubey, C., Radu, R., Schepers, D., Simmons, A., Soci, C., Abdalla, S., Abellan, X., Balsamo, G., Bechtold, P., Biavati, G., Bidlot, J., Bonavita, M., De Chiara, G., Dahlgren, P., Dee, D., Diamantakis, M., Dragani, R., Flemming, J., Forbes, R., Fuentes, M., Geer, A., Haimberger, L., Healy, S., Hogan, R. J., Hólm, E., Janisková, M., Keeley, S., Laloyaux, P., Lopez, P., Lupu, C., Radnoti, G., de Rosnay, P., Rozum, I., Vamborg, F., Villaume, S., and Thépaut, J.-N.: The ERA5 global reanalysis, Quarterly Journal of the Royal Meteorological Society, 146, 1999–2049, https://doi.org/https://doi.org/10.1002/qj.3803, 2020.

Heus, T., van Heerwaarden, C. C., Jonker, H. J. J., Siebesma, A. P., Axelsen, S., van den Dries, K., Geoffroy, O., Moene, A. F., Pino, D., de Roode, S. R., and de Arellano, J. V.-G.: Formulation of the Dutch Atmospheric Large-Eddy Simulation (DALES) and overview of its applications, Geoph. Model Dev., 3, 415–444, https://doi.org/10.5194/gmd-3-415-2010, 2010.

Huang, Y., Xia, Y., and Tan, X.: On the pattern of CO2 radiative forcing and poleward energy transport, Journal of Geophysical Research: Atmospheres, 122, 10,578–10,593, https://doi.org/https://doi.org/10.1002/2017JD027221, 2017.

Jensen, M., Giangrande, S., Fairless, T., and Zhou, A.: ARM Instrument: Interpolated Sonde (interpolatedsonde), ARM Research Facility [data set], https://doi.org/10.5439/1095316, 1998.

Jungclaus, J., Bittner, M., Wieners, K.-H., Wachsmann, F., Schupfner, M., Legutke, S., Giorgetta, M., Reick, C., Gayler, V., Haak, H., de Vrese, P., Raddatz, T., Esch, M., Mauritsen, T., von Storch, J.-S., Behrens, J., Brovkin, V., Claussen, M., Crueger, T., Fast, I., Fiedler, S., Hagemann, S., Hohenegger, C., Jahns, T., Kloster, S., Kinne, S., Lasslop, G., Kornblueh, L., Marotzke, J., Matei, D., Meraner, K., Mikolajewicz, U., Modali, K., Müller, W., Nabel, J., Notz, D., Peters-von Gehlen, K., Pincus, R., Pohlmann, H., Pongratz, J., Rast, S., Schmidt, H., Schnur, R., Schulzweida, U., Six, K., Stevens, B., Voigt, A., and Roeckner, E.: MPI-M MPIESM1.2-HR model output prepared for CMIP6 CMIP, Earth System Grid Federation [data set], https://doi.org/10.22033/ESGF/CMIP6.741, 2019.

Kahl, J. D.: Characteristics of the low-level temperature inversion along the Alaskan Arctic coast, International Journal of Climatology, 10, 537–548, https://doi.org/10.1002/joc.3370100509, 1990.

Kapsch, M.-L., Graversen, R. G., and Tjernström, M.: Springtime atmospheric energy transport and the control of Arctic summer sea-ice extent, Nature Climate Change, 3, 744–748, 2013.

Kern, S., Kaleschke, L., Girard-Ardhuin, F., Spreen, G., and Beitsch, A.: Global daily gridded 5-day median-filtered, gap-filled ASI Algorithm SSMI-SSMIS sea ice concentration data, Integrated Climate Date Center [data set], https://www.cen.uni-hamburg.de/en/icdc/data/cryosphere/seaiceconcentration-asi-ssmi.html, last access: 23 May 2022, 2020.

Koontz, A. and Uin, J.: AOS: Cloud Condensation Nuclei Counter (Dual Column), ramping mode averaged (aosccn2colaavg.b1), ARM Research Facility [data set], https://doi.org/10.5439/1323894, 2016.

Krasting, J. P., John, J. G., Blanton, C., McHugh, C., Nikonov, S., Radhakrishnan, A., Rand, K., Zadeh, N. T., Balaji, V., Durachta, J., Dupuis, C., Menzel, R., Robinson, T., Underwood, S., Vahlenkamp, H., Dunne, K. A., Gauthier, P. P., Ginoux, P., Griffies, S. M., Hallberg, R., Harrison, M., Hurlin, W., Malyshev, S., Naik, V., Paulot, F., Paynter, D. J., Ploshay, J., Reichl, B. G., Schwarzkopf, D. M., Seman, C. J., Silvers, L., Wyman, B., Zeng, Y., Adcroft, A., Dunne, J. P., Dussin, R., Guo, H., He, J., Held, I. M., Horowitz, L. W., Lin, P., Milly, P.,

https://doi.org/10.5194/acp-2022-836
Preprint. Discussion started: 9 January 2023

Shevliakova, E., Stock, C., Winton, M., Wittenberg, A. T., Xie, Y., and Zhao, M.: NOAA-GFDL GFDL-ESM4 model output prepared for CMIP6 CMIP, Earth System Grid Federation [data set], https://doi.org/10.22033/ESGF/CMIP6.1407, 2018.

Lauer, M., Block, K., Salzmann, M., and Quaas, J.: CO2-forced changes of Arctic temperature lapse-rates in CMIP5 models, Met. Z., 29, 79–93, https://doi.org/10.1127/metz/2020/0975, 2020.

Lawrence, Z. D., Perlwitz, J., Butler, A. H., Manney, G. L., Newman, P. A., Lee, S. H., and Nash, E. R.: The Remarkably Strong Arctic Stratospheric Polar Vortex of Winter 2020: Links to Record-Breaking Arctic Oscillation and Ozone Loss, Journal of Geophysical Research: Atmospheres, 125, e2020JD033 271, https://doi.org/10.1029/2020JD033271, e2020JD033271 10.1029/2020JD033271, 2020.

Linke, O. and Quaas, J.: The Impact of CO_2-Driven Climate Change on the Arctic Atmospheric Energy Budget in CMIP6 Climate Model Simulations, Tellus A: Dynamic Meteorology and Oceanography, 74, 2022.

Lu, J. and Cai, M.: Seasonality of polar surface warming amplification in climate simulations, Geophysical Research Letters, 36, 2009.

Lüpkes, C. and Schlünzen, K. H.: Meteorological measurements from 8 dropsondes released during POLAR 4 flight on 1993-03-04 along a track orthogonal to the pack ice edge north west of Svalbard, supplement to: Lüpkes, Christof; Schlünzen, K Heinke (1996): Modelling the arctic convective boundary-layer with different turbulence parameterizations. Boundary-Layer Meteorology, 79(1-2), 107-130, PANGAEA - Data Publisher for Earth & Environmental Science [data set], https://doi.org/10.1594/PANGAEA.857807, 1996.

Lüpkes, C., Hartmann, J., Schmitt, A. U., Birnbaum, G., Vihma, T., and Michaelis, J.: Airborne and dropsonde measurements in MCAOs during STABLE in March 2013, PANGAEA - Data Publisher for Earth & Environmental Science [data set], https://doi.org/10.1594/PANGAEA.936635, 2021.

Manabe, S. and Wetherald, R. T.: The Effects of Doubling the CO2 Concentration on the climate of a General Circulation Model, J. Atmos. Sci., 32, 3–15, https://doi.org/10.1175/1520-0469(1975)032<0003:TEODTC>2.0.CO;2, 1975.

Mather, J. H. and Voyles, J. W.: The Arm Climate Research Facility: A Review of Structure and Capabilities, Bulletin of the American Meteorological Society, 94, 377–392, https://doi.org/10.1175/bams-d-11-00218.1, 2013.

Maturilli, M., Holdridge, D. J., Dahlke, S., Graeser, J., Sommerfeld, A., Jaiser, R., Deckelmann, H., and Schulz, A.: Initial radiosonde data from 2019-10 to 2020-09 during project MOSAiC, PANGAEA - Data Publisher for Earth & Environmental Science [data set], https://doi.org/10.1594/PANGAEA.928656, 2021.

Melsheimer, C. and Spreen, G.: AMSR2 ASI sea ice concentration data, Arctic, version 5.4 (NetCDF) (July 2012 - December 2019), PANGAEA - Data Publisher for Earth & Environmental Science [data set], https://doi.org/10.1594/PANGAEA.898399, 2019.

Morrison, H., de Boer, G., Feingold, G., Harrington, J., Shupe, M. D., and Sulia, K.: Resilience of persistent Arctic mixed-phase clouds, Nat. Geosci., 5, 11–17, https://doi.org/doi.org/10.1038/NGEO1332, 2012.

NASA/GISS, N. G. I. f. S. S.: NASA-GISS GISS-E2.1G model output prepared for CMIP6 CMIP, Earth System Grid Federation [data set], https://doi.org/10.22033/ESGF/CMIP6.1400, 2018a.

NASA/GISS, N. G. I. f. S. S.: NASA-GISS GISS-E2.1H model output prepared for CMIP6 CMIP, Earth System Grid Federation [data set], https://doi.org/10.22033/ESGF/CMIP6.1421, 2018b.

Neggers, R. A. J., Siebesma, A. P., and Heus, T.: Continuous Single-Column Model Evaluation at a Permanent Meteorological Supersite, Bulletin of the American Meteorological Society, 93, 1389–1400, https://doi.org/10.1175/BAMS-D-11-00162.1, 2012.

Neggers, R. A. J., Chylik, J., Egerer, U., Griesche, H., Schemann, V., Seifert, P., Siebert, H., and Macke, A.: Local and Remote Controls on Arctic Mixed-Layer Evolution, Journal of Advances in Modeling Earth Systems, 11, 2214–2237, https://doi.org/10.1029/2019MS001671, 2019.

https://doi.org/10.5194/acp-2022-836
Preprint. Discussion started: 9 January 2023

Atmospheric Chemistry and Physics Discussions

Neubauer, D., Ferrachat, S., Siegenthaler-Le Drian, C., Stoll, J., Folini, D. S., Tegen, I., Wieners, K.-H., Mauritsen, T., Stemmler, I., Barthel, S., Bey, I., Daskalakis, N., Heinold, B., Kokkola, H., Partridge, D., Rast, S., Schmidt, H., Schutgens, N., Stanelle, T., Stier, P., Watson-Parris, D., and Lohmann, U.: HAMMOZ-Consortium MPI-ESM1.2-HAM model output prepared for CMIP6 CMIP, Earth System Grid Federation [data set], https://doi.org/10.22033/ESGF/CMIP6.1622, 2019.

Notz, D. and the SIMIP Community: Arctic Sea Ice in CMIP6, Geophys. Res. Lett., 47, e2019GL086 749, https://doi.org/https://doi.org/10.1029/2019GL086749, 2020.

Park, S. and Shin, J.: SNU SAM0-UNICON model output prepared for CMIP6 CMIP, Earth System Grid Federation [data set], https://doi.org/10.22033/ESGF/CMIP6.1489, 2019.

Pendergrass, A. G.: CAM5 Radiative Kernels, Climate Data at the National Center for Atmospheric Research [data set], https://doi.org/10.5065/D6F47MT6, 2017.

Pithan, F. and Mauritsen, T.: Arctic amplification dominated by temperature feedbacks in contemporary climate models, Nature geoscience, 7, 181–184, 2014.

Pithan, F., Svensson, G., Caballero, R., Chechin, D., Cronin, T. W., Ekman, A. M. L., Neggers, R., Shupe, M. D., Solomon, A., Tjernström, M., and Wendisch, M.: Role of air-mass transformations in exchange between the Arctic and mid-latitudes, Nature Geosci., 11, 805–812, https://doi.org/doi.org/10.1038/s41561-018-0234-1, 2018.

Reynolds, R. and Riihimaki, L.: Portable Radiation Package on Ice, ARM Research Facility [data set], https://doi.org/10.5439/1608608, 2019.

Ridley, J., Menary, M., Kuhlbrodt, T., Andrews, M., and Andrews, T.: MOHC HadGEM3-GC31-LL model output prepared for CMIP6 CMIP, Earth System Grid Federation [data set], https://doi.org/10.22033/ESGF/CMIP6.419, 2018.

Rüschendorf, L.: The Wasserstein distance and approximation theorems, Probability Theory and Related Fields, 70, 117–129, https://doi.org/10.1007/BF00532240, 1985.

Savita, A., Marsland, S., Dix, M., Bi, D., Dobrohotoff, P., Fiedler, R., Mackallah, C., Sullivan, A., Dias, F. B., Domingues, C. M., Hannah, N., Heerdegen, A., Hogg, A., and Druken, K.: CSIRO-ARCCSS ACCESS-CM2 model output prepared for CMIP6 FAFMIP, Earth System Grid Federation [data set], https://doi.org/10.22033/ESGF/CMIP6.2282, 2019.

Scoccimarro, E., Bellucci, A., and Peano, D.: CMCC CMCC-CM2-HR4 model output prepared for CMIP6 CMIP, Earth System Grid Federation [data set], https://doi.org/10.22033/ESGF/CMIP6.1358, 2020.

Seferian, R.: CNRM-CERFACS CNRM-ESM2-1 model output prepared for CMIP6 CMIP, Earth System Grid Federation [data set], https://doi.org/10.22033/ESGF/CMIP6.1391, 2018.

Seifert, A. and Beheng, K. D.: A two-moment cloud microphysics parameterization for mixed-phase clouds. Part 1: Model description, Meteorol. Atmos. Phys., 92, 45–66, https://doi.org/10.1007/s00703-005-0112-4, 2006.

Serreze, M. C. and Barry, R. G.: Processes and impacts of Arctic amplification: A research syn- thesis, Global Planet. Change, 77, 85–96, https://doi.org/10.1016/j.gloplacha.2011.03.004, 2011.

Shupe, M. D., Rex, M., Blomquist, B., Persson, P. O. G., Schmale, J., Uttal, T., Althausen, D., Angot, H., Archer, S., Bariteau, L., Beck, I., Bilberry, J., Bucci, S., Buck, C., Boyer, M., Brasseur, Z., Brooks, I. M., Calmer, R., Cassano, J., Castro, V., Chu, D., Costa, D., Cox, C. J., Creamean, J., Crewell, S., Dahlke, S., Damm, E., de Boer, G., Deckelmann, H., Dethloff, K., Dütsch, M., Ebell, K., Ehrlich, A., Ellis, J., Engelmann, R., Fong, A. A., Frey, M. M., Gallagher, M. R., Ganzeveld, L., Gradinger, R., Graeser, J., Greenamyer, V., Griesche, H., Griffiths, S., Hamilton, J., Heinemann, G., Helmig, D., Herber, A., Heuzé, C., Hofer, J., Houchens, T., Howard, D., Inoue, J., Jacobi, H.-W., Jaiser, R., Jokinen, T., Jourdan, O., Jozef, G., King, W., Kirchgaessner, A., Klingebiel, M., Krassovski, M., Krumpen, T., Lampert, A.,

https://doi.org/10.5194/acp-2022-836
Preprint. Discussion started: 9 January 2023

Landing, W., Laurila, T., Lawrence, D., Lonardi, M., Loose, B., Lüpkes, C., Maahn, M., Macke, A., Maslowski, W., Marsay, C., Maturilli, M., Mech, M., Morris, S., Moser, M., Nicolaus, M., Ortega, P., Osborn, J., Pätzold, F., Perovich, D. K., Petäjä, T., Pilz, C., Pirazzini, R., Posman, K., Powers, H., Pratt, K. A., Preußer, A., Quéléer, L., Radenz, M., Rabe, B., Rinke, A., Sachs, T., Schulz, A., Siebert, H., Silva, T., Solomon, A., Sommerfeld, A., Spreen, G., Stephens, M., Stohl, A., Svensson, G., Uin, J., Viegas, J., Voigt, C., von der Gathen, P., Wehner, B., Welker, J. M., Wendisch, M., Werner, M., Xie, Z., and Yue, F.: Overview of the MOSAiC expedition: Atmosphere, Elementa: Science of the Anthropocene, 10, https://doi.org/10.1525/elementa.2021.00060, 00060, 2022.

Smith, C. J., Kramer, R. J., and Sima, A.: The HadGEM3-GA7. 1 radiative kernel: the importance of a well-resolved stratosphere, Earth System Science Data, 12, 2157–2168, 2020.

Soden, B. J. and Held, I. M.: An assessment of climate feedbacks in coupled ocean–atmosphere models, Journal of climate, 19, 3354–3360, 2006.

Stengel, M., Stapelberg, S., Sus, O., Finkensieper, S., Würzler, B., Philipp, D., Hollmann, R., Poulsen, C., Christensen, M., and McGarragh, G.: Cloud_cci Advanced Very High Resolution Radiometer post meridiem (AVHRR-PM) dataset version 3: 35-year climatology of global cloud and radiation properties, Earth System Science Data, 12, 41–60, https://doi.org/10.5194/essd-12-41-2020, 2020.

Stevens, B., Moeng, C.-H., Ackerman, A. S., Bretherton, C. S., Chlond, A., de Roode, S., Edwards, J., Golaz, J.-C., Jiang, H., Khairoutdinov, M., Kirkpatrick, M. P., Lewellen, D. C., Lock, A., Müller, F., Stevens, D. E., Whelan, E., and Zhu, P.: Evaluation of Large-Eddy Simulations via Observations of Nocturnal Marine Stratocumulus, Monthly Weather Review, 133, 1443 – 1462, https://doi.org/10.1175/MWR2930.1, 2005.

Tang, Y., Rumbold, S., Ellis, R., Kelley, D., Mulcahy, J., Sellar, A., Walton, J., and Jones, C.: MOHC UKESM1.0-LL model output prepared for CMIP6 CMIP, Earth System Grid Federation [data set], https://doi.org/10.22033/ESGF/CMIP6.1569, 2019.

Tatebe, H. and Watanabe, M.: MIROC MIROC6 model output prepared for CMIP6 CMIP, Earth System Grid Federation [data set], https://doi.org/10.22033/ESGF/CMIP6.881, 2018.

Taylor, P. C., Cai, M., Hu, A., Meehl, J., Washington, W., and Zhang, G. J.: A Decomposition of Feedback Contributions to Polar Warming Amplification, Journal of Climate, 26, 7023 – 7043, https://doi.org/10.1175/JCLI-D-12-00696.1, 2013.

Van Laar, T. W., Schemann, V., and Neggers, R. A. J.: Investigating the diurnal evolution of the cloud size distribution of continental cumulus convection using multi-day LES, J. Atmos. Sci., https://doi.org/10.1175/JAS-D-18-0084.1, 2019.

Voldoire, A.: CNRM-CERFACS CNRM-CM6-1 model output prepared for CMIP6 CMIP, Earth System Grid Federation [data set], https://doi.org/10.22033/ESGF/CMIP6.1375, 2018.

Voldoire, A.: CNRM-CERFACS CNRM-CM6-1-HR model output prepared for CMIP6 CMIP, Earth System Grid Federation [data set], https://doi.org/10.22033/ESGF/CMIP6.1385, 2019.

Volodin, E., Mortikov, E., Gritsun, A., Lykossov, V., Galin, V., Diansky, N., Gusev, A., Kostrykin, S., Iakovlev, N., Shestakova, A., and Emelina, S.: INM INM-CM5-0 model output prepared for CMIP6 CMIP, Earth System Grid Federation [data set], https://doi.org/10.22033/ESGF/CMIP6.1423, 2019a.

Volodin, E., Mortikov, E., Gritsun, A., Lykossov, V., Galin, V., Diansky, N., Gusev, A., Kostrykin, S., Iakovlev, N., Shestakova, A., and Emelina, S.: INM INM-CM4-8 model output prepared for CMIP6 PMIP, Earth System Grid Federation [data set], https://doi.org/10.22033/ESGF/CMIP6.2295, 2019b.

Wendisch, M., Brückner, M., Crewell, S., Ehrlich, A., Notholt, J., Lüpkes, C., Macke, A., Burrows, J. P., Rinke, A., Quaas, J., Maturilli, M., Schemann, V., Shupe, M., Barrientos-Velasco, C., Barfuss, K., Blechschmidt, A., Block, K., Bougoudis, I., Bozem, H., Böckmann, C., Bracher, A., Bresson, H., Bretschneider, I., Buschmann, M., Chechin, D., Chylik, J., Dahlke, S., Deneke, H., Dethloff, K., Donth, T., Dorn,

https://doi.org/10.5194/acp-2022-836
Preprint. Discussion started: 9 January 2023

W., Dupuy, R., Ebell, K., Egerer, U., Engelmann, R., Eppers, O., Gerdes, R., Gierens, R., Gorodetskaya, I., Gottschalk, M., Griesche, H., Gryanik, V., Handorf, D., Altstädter, B., Hartmann, J., Hartmann, M., Heinold, B., Herber, A., Herrmann, H., Heygster, G., Höschel, I., Hofmann, Z., Hölemann, J., Hünerbein, A., Jafariserajehlou, S., Jäkel, E., Jacobi, C., Janout, M., Jansen, F., Jourdan, O., Juranyi, Z., Kalesse-Los, H., Kanzow, T., Käthner, R., Kliesch, L., Klingebiel, M., Knudsen, E., Kovacs, T., Körtke, W., Krampe, D., Kretzschmar, J., Kreyling, D., Kulla, B., Kunkel, D., Lampert, A., Lauer, M., Lelli, L., Annakaisa von L., Linke, O., Loehnert, U., Lonardi, M., Losa, S., Losch, M., Maahn, M., Mech, M., Mei, L., Mertes, S., Metzner, E., Mewes, D., Michaelis, J., Mioche, G., Moser, M., Nakoudi, K., Neggers, R., Neuber, R., Nomokonova, T., Oelker, J., Papakonstantinou-Presvelou, I., Pätzold, F., Pefanis, V., Pohl, C., Manuela van P., Radovan, A., Rhein, M., Rex, M., Richter, A., Risse, N., Ritter, C., Rostosky, P., Rozanov, V., Ruiz-Donoso, E., Saavedra, P., Salzmann, M., Schacht, J., Schäfer, M., Schneider, J., Schnierstein, N., Seifert, P., Seo, S., Siebert, H., Soppa, M., Spreen, G., Stachlewska, I., Stapf, J., Stratmann, F., Tegen, I., Viceto, C., Voigt, C., Vountas, M., Walbroel, A., Walter, M., Wehner, B., Wex, H., Willmes, S., Zanatta, M., and Zeppenfeld, S.: Atmospheric and Surface Processes, and Feedback Mechanisms Determining Arctic Amplification: A Review of First Results and Prospects of the $(AC)^3$ Project, Bull. Amer. Meteorol. Soc., online early, https://doi.org/10.1175/BAMS-D-21-0218.1, 2022.

Wieners, K.-H., Giorgetta, M., Jungclaus, J., Reick, C., Esch, M., Bittner, M., Legutke, S., Schupfner, M., Wachsmann, F., Gayler, V., Haak, H., de Vrese, P., Raddatz, T., Mauritsen, T., von Storch, J.-S., Behrens, J., Brovkin, V., Claussen, M., Crueger, T., Fast, I., Fiedler, S., Hagemann, S., Hohenegger, C., Jahns, T., Kloster, S., Kinne, S., Lasslop, G., Kornblueh, L., Marotzke, J., Matei, D., Meraner, K., Mikolajewicz, U., Modali, K., Müller, W., Nabel, J., Notz, D., Peters-von Gehlen, K., Pincus, R., Pohlmann, H., Pongratz, J., Rast, S., Schmidt, H., Schnur, R., Schulzweida, U., Six, K., Stevens, B., Voigt, A., and Roeckner, E.: MPI-M MPIESM1.2-LR model output prepared for CMIP6 CMIP, Earth System Grid Federation [data set], https://doi.org/10.22033/ESGF/CMIP6.742, 2019.

Woods, C., Caballero, R., and Svensson, G.: Large-scale circulation associated with moisture intrusions into the Arctic during winter, Geophys. Res. Lett., 40, 4717–4721, 2013.

Xin, X., Zhang, J., Zhang, F., Wu, T., Shi, X., Li, J., Chu, M., Liu, Q., Yan, J., Ma, Q., and Wei, M.: BCC BCC-CSM2MR model output prepared for CMIP6 CMIP, Earth System Grid Federation [data set], https://doi.org/10.22033/ESGF/CMIP6.1725, 2018.

Yang, W. and Magnusdottir, G.: Springtime extreme moisture transport into the Arctic and its impact on sea ice concentration, Journal of Geophysical Research: Atmospheres, 122, 5316–5329, https://doi.org/10.1002/2016JD026324., 2017.

Yu, Y.: CAS FGOALS-f3-L model output prepared for CMIP6 CMIP, Earth System Grid Federation [data set], https://doi.org/10.22033/ESGF/CMIP6.1782, 2018.

Yukimoto, S., Koshiro, T., Kawai, H., Oshima, N., Yoshida, K., Urakawa, S., Tsujino, H., Deushi, M., Tanaka, T., Hosaka, M., Yoshimura, H., Shindo, E., Mizuta, R., Ishii, M., Obata, A., and Adachi, Y.: MRI MRI-ESM2.0 model output prepared for CMIP6 CMIP, Earth System Grid Federation [data set], https://doi.org/10.22033/ESGF/CMIP6.621, 2019.

Ziehn, T., Chamberlain, M., Lenton, A., Law, R., Bodman, R., Dix, M., Wang, Y., Dobrohotoff, P., Srbinovsky, J., Stevens, L., Vohralik, P., Mackallah, C., Sullivan, A., O'Farrell, S., and Druken, K.: CSIRO ACCESS-ESM1.5 model output prepared for CMIP6 CMIP, Earth System Grid Federation [data set], https://doi.org/10.22033/ESGF/CMIP6.2288, 2019.

https://doi.org/10.5194/acp-2022-836
Preprint. Discussion started: 9 January 2023

Atmospheric Chemistry and Physics Discussions

Table 1. All CMIP6 models used in this study with AA and ALRF derived from the surface-near atmospheric temperature, and lapse-rate difference, respectively, between 1985–2014 and 1951–1980. Table 1 further gives the time resolution available in the model diagnostics (6h: 6-hourly, day: daily, mon: monthly), together with the categorisation as weak or strong-AA models (CMIP6/w or CMIP6/s; in the superscript of the acronyms) per time-resolution group. Bold model acronyms indicate models that are most skilled at simulating a realistic amount of sea-ice loss together with a plausible global temperature change over time according to Notz and the SIMIP Community (2020).

	Model acronym	AA / K	ALRF / K	Time resolution	Reference
1	INM-CM5-0$^{\text{day, CMIP6/w}}$	0.210	0.067	day	Volodin et al. (2019a)
2	INM-CM4-8$^{\text{day, CMIP6/w}}$	0.241	0.094	day	Volodin et al. (2019b)
3	**GFDL-ESM4**$^{\text{mon, CMIP6/w}}$	0.274	0.103	mon	Krasting et al. (2018)
4	HadGEM3-GC31-LL$^{\text{day, mon, CMIP6/w}}$	0.549	0.143	day, mon	Ridley et al. (2018)
5	SAM0-UNICON$^{\text{6h, mon, CMIP6/w}}$	0.552	0.271	6h, mon	Park and Shin (2019)
6	**MPI-ESM-1-2-HAM**$^{\text{6h, CMIP6/w}}$	0.641	0.176	6h, day, mon	Neubauer et al. (2019)
7	CMCC-CM2-HR4	0.642	0.270	day, mon	Scoccimarro et al. (2020)
8	**ACCESS-CM2**	0.668	0.176	mon	Savita et al. (2019)
9	MIROC-ES2L	0.678	0.215	mon	Hajima et al. (2019)
10	AWI-ESM-1-1-LR$^{\text{6h, CMIP6/w}}$	0.689	0.283	6h, day	Danek et al. (2020)
11	**NorESM2-MM**	0.695	0.235	6h	Bentsen et al. (2019)
12	CESM2-FV2	0.729	0.166	day, mon	Danabasoglu (2019a)
13	**BCC-CSM2-MR**	0.743	0.258	mon	Xin et al. (2018)
14	CNRM-CM6-1	0.743	0.298	6h, day, mon	Voldoire (2018)
15	**MPI-ESM1-2-LR**	0.751	0.256	6h, day, mon	Wieners et al. (2019)
16	MIROC6	0.769	0.246	6h	Tatebe and Watanabe (2018)
17	ACCESS-ESM1-5	0.787	0.200	mon	Ziehn et al. (2019)
18	**GISS-E2-1-G**	0.814	0.306	6h	NASA/GISS (2018a)
19	UKESM1-0-LL	0.817	0.265	day, mon	Tang et al. (2019)
20	NESM3	0.824	0.296	mon	Cao and Wang (2019)
21	**MPI-ESM1-2-HR**	0.830	0.312	6h, day	Jungclaus et al. (2019)
22	CESM2-WACCM-FV2	0.867	0.236	day, mon	Danabasoglu (2019b)
23	GFDL-CM4	0.875	0.258	day, mon	Guo et al. (2018)
24	CESM2-WACCM	0.933	0.253	day, mon	Danabasoglu (2019c)
25	CNRM-ESM2-1$^{\text{6h, CMIP6/s}}$	0.956	0.374	6h, day, mon	Seferian (2018)
26	**FGOALS-f3-L**	0.960	0.419	mon	Yu (2018)
27	CESM2	0.993	0.286	day, mon	Danabasoglu (2019d)
28	**CNRM-CM6-1-HR**$^{\text{6h, day, CMIP6/s}}$	1.002	0.372	6h, day, mon	Voldoire (2019)
29	IPSL-CM6A-LR$^{\text{6h, day, mon, CMIP6/s}}$	1.062	0.378	6h, day, mon	Boucher et al. (2018)
30	**MRI-ESM2-0**$^{\text{day, mon, CMIP6/s}}$	1.116	0.338	day, mon	Yukimoto et al. (2019)
31	GISS-E2-1-H$^{\text{mon, CMIP6/s}}$	1.148	0.490	mon	NASA/GISS (2018b)